



LUT
Lappeenranta
University of Technology

Päivi Sikiö

DYNAMICAL TREE MODELS FOR HIGH REYNOLDS NUMBER TURBULENCE APPLIED IN FLUID-SOLID SYSTEMS OF 1D-SPACE AND TIME

Thesis for the degree of Doctor of Science (Technology) to be presented with due permission for public examination and criticism in the Auditorium 6311 at Lappeenranta University of Technology, Lappeenranta, Finland on the 13th of December 2017, at noon.

Acta Universitatis
Lappeenrantaensis 780

Supervisors Docent Payman Jalali
LUT School of Energy Systems
Lappeenranta University of Technology
Finland

Docent Tero Tynjälä
LUT School of Energy Systems
Lappeenranta University of Technology
Finland

Reviewers Professor Luca Biferale
Department of Physics
University of Rome
Italy

Professor Suad Jakirlic
Department of Mechanical Engineering
Technische Universität Darmstadt
Germany

Opponent Ph.D. University Researcher Paolo Muratore-Ginanneschi
Department of Mathematics and Statistics
University of Helsinki
Finland

ISBN 978-952-335-182-0
ISBN 978-952-335-183-7 (PDF)
ISSN-L 1456-4491
ISSN 1456-4491

Lappeenrannan teknillinen yliopisto
LUT Yliopistopaino 2017

Abstract

Päivi Sikiö

Dynamical tree models for high Reynolds number turbulence applied in fluid-solid systems of 1D-space and time

Lappeenranta 2017

79 pages

Acta Universitatis Lappeenrantaensis 780

Diss. Lappeenranta University of Technology

ISBN 978-952-335-182-0, ISBN 978-952-335-183-7 (PDF), ISSN-L 1456-4491,

ISSN 1456-4491

A modified hierarchical spatiotemporal dynamical system model (tree model) is utilized to study turbulence modulation caused due to the insertion of a dispersed phase particle in turbulent field. Multiscale nature of the problem combined with the interaction among different phases makes the handling of turbulent dispersed phase multiphase flows intricate and computationally costly. Navier-Stokes equations, describing the turbulent flow evolution are highly complex for numerical solution techniques and even more challenge is added in case of high Reynolds numbers. Shell models are simplified dynamical models, which imitate the behaviour of the Navier-Stokes equations in time domain. They are capable of capturing many fundamental features of turbulence, such as the intermittency and the anomalous scaling of the turbulent energy cascade mechanism, with striped-down system of coupled nonlinear ordinary differential equations. They offer an efficient tool for studying the high Reynolds number turbulence. The focus of this work is the utilization of a hierarchical shell model, a tree model with one spatial dimension and time, for the study of turbulent energy dissipation rate in the direct vicinity of dispersed phase particle. Tree models put forward a new approach in handling the particle-turbulent field interface enabling both temporal and spatial fluctuations of turbulent energy cascade in high Reynolds number cases. In this thesis work, for the first time, a solid particle is applied in those models to study the distribution of the energy dissipation reproduced by common dynamical models of turbulence. Two different tree models, namely A and B, are considered, which have different number of nonlinear interactions. The models are modified to take into account the presence of dispersed phase. The model performance is studied, as different sizes of particles larger than Kolmogorov length scale are inserted in sustained or decaying turbulence. The study of time-averaged spatially resolved energy dissipation rate shows local augmentation near the particle surface compared to the farther locations. The amount of the augmentation is found to be proportionally dependent of the size of the particle, and it is effective in the range of 1-1.5 particle diameters from the particle surface. The results are compared to the studies found in literature. For comparison, also some computational fluid dynamics (CFD) simulations are performed using the computer package of ANSYS-Fluent. Furthermore, shell model simulations are performed with dual particles separated by certain distances of one to three particle diameters in forced turbulence. Dissipation escalation is detected at the particle surfaces. The energy dissipation rate in the mid-distance of the particles is found to be lower than that at the particle surfaces and it

decreases as the distance between particles increases. Furthermore, simulations with variable Reynolds number, $Re \sim 1/\nu$ as 10^4 , 5×10^4 , and 10^6 , are studied for unladen and particle laden cases. Larger dissipation rise near particle surface is observed for smaller Re , when the particle size is the same compared to the Kolmogorov length scale. If the physical particle size is kept the same, dissipation rise at the particle surface is found to be similar for different Reynolds numbers. Velocity field structure functions are employed to study the scaling properties of the model with particle insertions using extended self-similarity (ESS) method to find the scaling exponents of the structure functions. Results are compared to the unladen case and the values from literature. Intermittency was detected in unladen and laden simulations of both models A and B. For model A, higher levels of intermittency were discovered in comparison to model B. The comparison of simulations using model B with variable particle sizes revealed larger degree of intermittency in larger particle sizes. The impact of the current research is in introducing a new insight into the numerical modelling of highly turbulent flows in two-phase flows, which are computationally challenging or costly using conventional CFD techniques.

Keywords: Dynamical system approach; Hierarchical shell model; Spatiotemporal tree model; Dispersed phase multiphase system; High Reynolds number turbulence; Turbulent energy dissipation

Acknowledgements

This work was carried out in the Laboratory of Thermodynamics of LUT School of Energy Systems at Lappeenranta University of Technology, Finland. I wish to express my sincere appreciation to those who have contributed to this thesis and supported me during this work.

Foremost, I would like to express my deep and sincere gratitude to my research supervisors, Associate Professors Payman Jalali and Tero Tynjälä, for their patient and motivating guidance and continuous support of my Ph.D study and research. I am also thankful for them for the privilege of being given the opportunity to study such a remarkable and fascinating universal phenomenon as turbulence.

My sincere thanks go to Professor Pertti Sarkomaa, the former Head of the Laboratory of Thermodynamics, for inspiring me and giving me the impact on the path of research work.

I appreciatively acknowledge the preliminary examiners Professor Luca Biferale and Suad Jakirlic, for their insightful comments and suggestions, which helped to improve the presentation of the thesis.

I would like to say thanks to my friends and research colleagues, with special thanks to Anne Jordan, Aija Kivistö and Mahsa Dabagh, for their supporting friendship during all these years we've known.

I gratefully acknowledge the funding support for my Ph.D. work provided by the Academy of Finland and Tekniikan Edistämissäätiö.

I would also like to thank my parents, who always hope and pray the best for me, and my brothers and sister, for believing in me. My mother and my mother in law deserve special thanks for taking care of the children.

Finally, I would like to thank those closest to me, my children Joni, Henna, Sini and Elina, for keeping my feet on the ground and focus on the most important things, and for giving me the reason to carry on my work through the hard times. I want to thank Ykä, without whom I would not be where I am today.

Päivi Sikiö
November 2017
Lappeenranta, Finland

Contents

Abstract

Acknowledgements

Contents

List of publications	9
Nomenclature	11
1 Introduction	15
2 State of the art	19
2.1 Turbulence.....	19
2.1.1 Turbulence as a phenomenon.....	19
2.1.2 Basic characteristics of turbulence.....	20
2.1.3 Turbulence as a dynamical system.....	22
2.1.4 Turbulence modelling	24
2.1.5 Turbulent modulation in dispersed phase two phase flow	25
2.2 Shell models of turbulence	29
2.2.1 GOY shell model	29
2.2.2 Helical shell models	30
2.2.3 Spatio-temporal tree model.....	30
3 Methods	33
3.1 Theory and formulation.....	33
3.1.1 The tree model	33
3.1.2 Energy dissipation.....	35
3.1.3 Inclusion of dispersed phase particle into the tree model	41
3.2 Numerical implementation	41
4 Results	43
4.1 Performance of the tree model	43
4.2 Scaling properties of the model.....	45
4.2.1 Unladen and particle laden cases of models A and B	46
4.2.2 Scaling of the model with different size particles.....	51
4.2.3 Effect of Reynolds number variation	51
4.3 Dissipation.....	54
4.3.1 Particle size variation: Model A.....	54
4.3.2 Particle size variation: Model B.....	58
4.3.3 Particle pairs.....	62
4.3.4 Variable Reynolds number.....	65
5 Conclusions	71
References	75

List of publications

This thesis contains material from the following papers. The rights have been granted by publishers to include the material in dissertation.

P. Sikiö, and P. Jalali (2014). Study of turbulent energy dissipation rate of fluid flow in the vicinity of dispersed phase boundary using spatiotemporal tree model. *Chaos* 24(4), pp. 043139:1-11.

P. Sikiö, T. Tynjälä, and P. Jalali (2017a). A spatiotemporal tree model for turbulence in dispersed phase multiphase flows: Energy dissipation rate (EDR) behavior in single particle and binary particles arrays. *Chaos* 27, pp. 013102:1-10.

P. Sikiö, T. Tynjälä, and P. Jalali (2017b). Effect of particle size on scaling properties of turbulence: Shell model approach. Submitted for journal publication.

P. Sikiö, T. Tynjälä, and P. Jalali (2017c). Turbulent energy dissipation rate modification due to particle insertion: Effect of Reynolds number. Submitted for journal publication.

Nomenclature

In the present work, variables and constants are denoted using *slanted style*, vectors are denoted using **bold regular style**, and abbreviations are denoted using regular style.

Latin alphabet

a	constant	—
b	constant	—
c	constant	—
D	energy dissipation moment	—
d	constant	—
d_P	dimensionless particle diameter	—
E	dimensionless energy	—
e	constant	—
F	dimensionless force	—
f	constant	—
H	dimensionless helicity	—
i	imaginary unit	—
j	spatial index	—
k	wavenumber	—
L	characteristic length	m
L_d	dimensionless domain length	—
l	dimensionless length scale	—
l_I	integral length scale	—
l_K	Kolmogorov length scale	—
N	total number of shells	—
n	shell number	—
p	order of moment	—
\mathbf{r}	space vector	—
r	length of \mathbf{r}	—
S	velocity structure function	—
T	number of time steps	—
t	dimensionless time	—
U	velocity	m/s
u	dimensionless velocity	—
x	x-coordinate (width)	—
Z	dimensionless enstrophy	—

Greek alphabet

α	constant	—
β	constant	—
δ	difference	—
$\delta_{i,j}$	Kronecker delta	—
ε, ϵ	dimensionless energy dissipation rate	—
ζ	scaling exponent	—
η	dimensionless energy dissipation density	—
λ	shell spacing parameter	—
ν	dimensionless kinematic viscosity	—
Σ	sum	—
τ	eddy turnover time	-
ψ	wavelet	-
ω	specific rate of dissipation of turbulent kinetic energy	1/s

Dimensionless numbers

Re	Reynolds number
------	-----------------

Superscripts

s	helicity sign
$*$	complex conjugate
$'$	neighbor
$''$	second neighbor

Subscripts

abs	absolute value
I	integral (length scale)
K	Kolmogorov (length scale)
P	particle
T	Taylor microscale
ref	reference

Abbreviations

1D	one dimensional
2D	two dimensional
3D	three dimensional
ca	circa
CFD	computational fluid dynamics
DES	detached eddy simulation
DNS	direct numerical simulation

GOY	Gledzer-Ohkitani-Yamada (model)
IBM	immersed boundary method
JPL	Jet Propulsion Laboratory
K41	Kolmogorov's theory of 1941
LES	large eddy simulation
log	logarithm
MSSS	Malin Space Science Systems
NASA	National Aeronautics and Space Administration
NS	Navier-Stokes
ODE	ordinary differential equation
PIV	particle image velocimetry
pdf	probability density function
RANS	Reynolds averaged Navier-Stokes
SwRI	Southwest Research Institute
URANS	unsteady RANS

1 Introduction

The complexity in the modeling of particulate turbulent multiphase flows arises from the broad band of spatial and temporal scales involved compounded with the interaction among phases, especially in case of high Reynolds numbers. The solution process of the Navier-Stokes equations is very challenging and computationally costly. Shell models offer a new unique perspective to high Reynolds number turbulence in dispersed phase multiphase systems. Imitating the Navier-Stokes equations, shell models capture the fundamental characteristics of turbulence, such as intermittency and the anomalous scaling of the energy cascade with reduced number of degrees of freedom to solve.

The main issue throughout the extensive research field of turbulent multiphase flow systems existing in nature, biology and engineering, is the need to develop models capable of capturing the details of flow to understand the mutual effects of phases. Achieving such knowledge in dispersed phase flows will yield important practical applications that can potentially increase the efficiency, lower the cost, advance the safety and reduce the pollutant emissions in industry. The models for turbulent multiphase flows can be examined through laboratory-scale experiments, computationally harnessing the calculation power of supercomputers to solve the complexities of the flow field or theoretically by using the analytical solution of mathematical equations. The advantages and challenges in experimental, numerical and theoretical studies of the particle-turbulence interaction dynamics are addressed by Balachandar and Eaton (2010) and Bourgoin and Xu (2014). Experiments are designed for specific cases and the generalization is not always straight forward. Also, the experimental measurements in two phases are not trivial. Especially, the carrier-phase velocity close to the particle surface and the energy dissipation rate are challenges for any experimental measurements. Computational methods play the major role in handling the multiphase flow applications. Computational resources needed for solving full Navier-Stokes equations for all the phases in turbulent multiphase flows are extremely costly, which seems to be out of reach for decades despite the rapid progress in computational power. Direct numerical simulation (DNS) techniques have been developed to solve the motion of fluid around individual particles. However, in real natural systems and engineering applications, DNS techniques are restricted to rather low Reynolds numbers. Therefore, simplifications are needed in modelling of turbulent multiphase flows. A thorough understanding of the turbulent dynamics of individual particles is necessary for the development of turbulent multiphase flow modelling.

Modulation of local dissipation properties in the turbulent field due to the particle insertion is one of the main effects of particles on the turbulence (Saber et al. 2015). A few studies in the broad research field of multiphase flows have concentrated on the turbulence modulation in the vicinity of particle surface. These experimental and numerical simulation studies regarding the turbulent energy dissipation modulation due to the finite size particles in turbulent field are reviewed in Chapter 2 and summarized in Table 1. Burton and Eaton (2005) performed a DNS study of a single particle in decaying turbulence and found enhanced dissipation near particle surface about 20% higher than

that of unladen case. In this thesis, the turbulent hierarchical spatiotemporal dynamical system model (tree model) with one spatial dimension is investigated for the energy dissipation fluctuations in the presence of spatially localized obstacle in case of high Reynolds numbers. The hierarchical shell models, capable of reaching high Reynolds numbers, offer a new fascinating perspective to dispersed phase multiphase flows. Shell models are phenomenological models developed to capture the turbulent energy cascade in high Reynolds numbers with stripped-down system of coupled nonlinear ordinary differential equations. A spatial dimension is achieved by transforming the original chain model to a tree model with hierarchical structure, which makes the shell model suitable for investigating local dissipation effects caused by dispersed particles located in turbulent field. The objective of this work is to investigate a hierarchical shell model for the modulation of the energy dissipation fluctuations on the small-scales, caused by spatially localized particle, which blocks the energy from flowing to smaller and smaller scales.

The model utilized in this thesis is the turbulent hierarchical shell model proposed by Benzi et al. (1997) with the modification made to take into account the insertion of finite size dispersed phase particle. Two models, namely model A and model B, with variable interaction ranges in physical dimension are being considered. The effect of particle size on the dissipation signal, along with the scaling properties of turbulence with particle insertion, is studied through model simulations for long enough time spans (Sikiö and Jalali 2014, Sikiö et al. 2017a, Sikiö et al. 2017b). Also, particle pairs are studied for the mutual interaction of the particles in turbulent model domain separated by certain distances (Sikiö et al. 2017a). Furthermore, particle laden simulations with variable Reynolds number, $Re \sim 1/\nu$ as 10^4 , 5×10^4 , and 10^6 , are investigated (Sikiö et al. 2017c). As the major part of the content of this thesis is published in papers (Sikiö and Jalali 2014, Sikiö et al. 2017a, Sikiö et al. 2017b, Sikiö et al. 2017c), it should be remarked, that P. Sikiö has been the corresponding author of all papers. The simulation code was substantially developed by P. Sikiö with the supervision of Dr. Jalali, who continuously supervised via discussions for planning and analysing simulations, their results and postprocessing. In the first paper (Sikiö and Jalali 2014), Dr. Jalali contributed in developing the scope of the paper and also commenting prior to the submissions to the journal. In all other papers (Sikiö et al. 2017a, Sikiö et al. 2017b, Sikiö et al. 2017c), Dr. Jalali and Dr. Tynjälä both contributed in all stages from planning the scope to the pre-submission reviews of the articles. The contribution of P. Sikiö was to conduct the simulations and analysing and postprocessing of the simulation data with writing the papers.

This thesis is organized as follows. Chapter 2 provides a quick glance to the research field associated with this thesis including a brief literature review of the present knowledge of the turbulence modification by dispersed phase particles. In Chapter 3, the two models used in this work are described in details and the modifications for the insertion of the dispersed phase particle in the models are explained. Also, the energy dissipation quantities used in the study are delineated and numerical implementation for the studied cases is presented. Chapter 4 introduces the results of the studied cases with discussions

of the scaling properties of the turbulence produced by the models in unladen and particle laden simulations, and the energy dissipation rate modifications due to the particle insertions. Finally, conclusions appear in Chapter 5.

2 State of the art

2.1 Turbulence

2.1.1 Turbulence as a phenomenon

Turbulence is an intriguing challenge studied over a century (Lumley and Yaglom 2001). Turbulence is chaotic, irregular, unpredictable, irreversible disorder, yet statistically well-organized containing eddies, that constitute a hierarchy over a wide range of scales. It exists in numerous examples in nature and engineering applications. It is astonishing, how this complex phenomenon can be encountered in very different systems at huge range of scales, starting from galaxies and solar system, through atmospheric and oceanic scales as well as various industrial scale flows, up to the scale of blood flow in the human body. Figure 2.1. shows the giant turbulent streams in the atmosphere of Jupiter (NASA/JPL-Caltech/SwRI/MSSS/Sergey Dushkin 2017), as a classic natural example of turbulent flows found in a gas giant. Geophysical turbulence is essential, when it comes to the prediction of atmospheric and oceanic phenomena, such as the motion of water in creeks, rivers and ocean currents, cloud formation in the atmosphere or for instance volcanic eruption. Turbulence is to be considered also in multiple engineering flow applications, like flow around submarine, automobiles and aircraft wings, industrial pipe flows, mixing of fuel and air in combustion process, or cooling enhancement in engineering systems. It also affects biological systems, like speech production or cardiovascular system.

Complexity of turbulence phenomenon arises from the random, chaotic, and highly unpredictable behaviour of flow quantities, such as velocity and pressure at wide-ranging temporal and spatial scales. Intricacy is even increased, when a second phase is added in the flow. Our interest is in turbulent dispersed phase multiphase flows, meaning a continuous fluid phase laden with particles, drops or bubbles. Interaction between dispersed phase elements and turbulence plays an important role in a variety of turbulent applications occurring in nature and technology. Examples in our environment include formation of rain and snow, sediment transport in rivers and seas, avalanches and mud slides, sand storms, clouds and the transport of pollutants in the atmosphere. Understanding the properties of these flows and the interaction between the dispersed phase and the fluid phase can help in predicting and controlling these environmental phenomena. Technical and industrial applications are countless, such as pneumatic conveying systems, chemical engineering, food and medical applications, energy production systems, including fluidized bed combustion, fuel injection in engines, gasification of organic or fossil fuel, vapour generators and heat exchangers. Prediction of these flows is essential in improving these industrial processes and energy efficiency or reducing pollutant emissions of the processes.

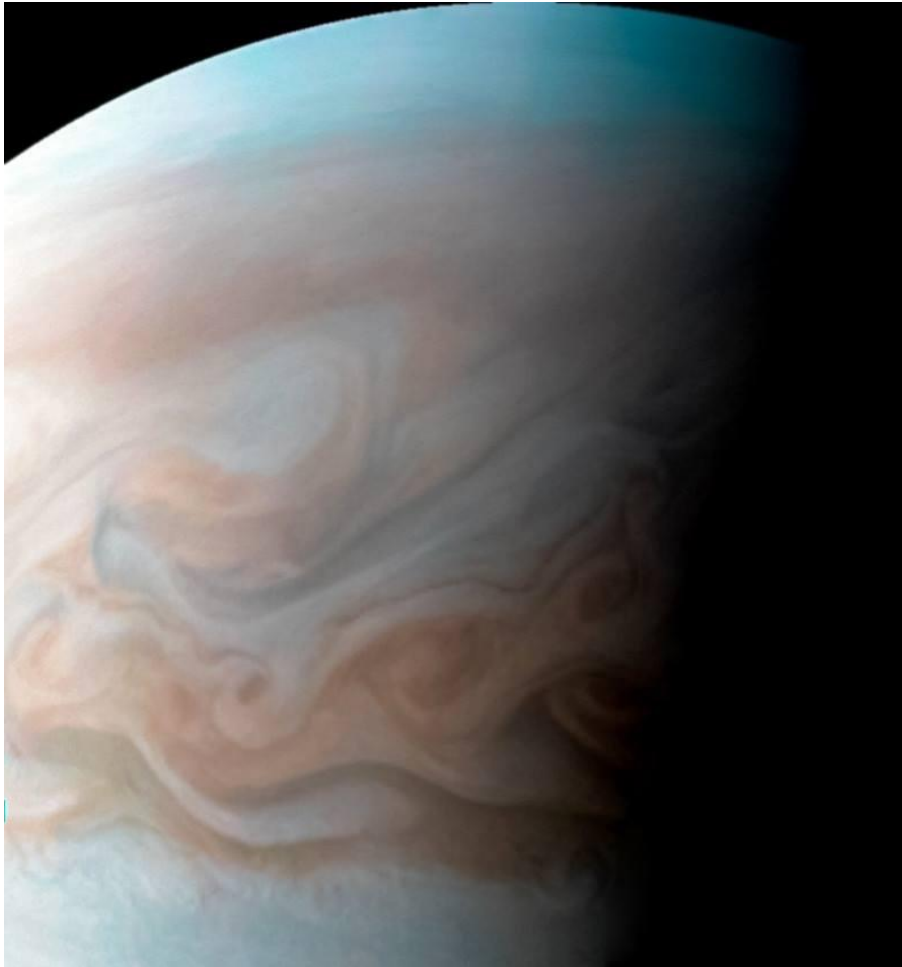


Figure 2.1: Turbulent storm patterns in the atmosphere of Jupiter taken by NASA's Juno spacecraft. NASA/JPL-Caltech/SwRI/MSSS/Sergey Dushkin 2017.

2.1.2 Basic characteristics of turbulence

Transition from a smooth, regular and constant fluid motion, namely laminar flow towards turbulent disordered regime takes place when Reynolds number Re of the flow grows sufficiently. Reynolds number is a dimensionless quantity brought out by Osborne Reynolds in the 19th century through experimental studies (Reynolds 1883), defined as the ratio of the inertial forces to the viscous forces

$$Re=UL/\nu, \quad (2.1)$$

where U and L are velocity and characteristic length of the flow, respectively and ν is the kinematic viscosity. Reynolds number is independent of the scale of the flow.

Besides disorder and irregularity, another characteristic feature of turbulence is the formation of eddies at the length scales of the flow boundaries (largest scales) along with the intermediate and smaller scales. In fact, vortical structures in turbulent flow were pictured by Leonardo da Vinci nearly 400 years before Reynolds, as presented in Fig. 2.2. Leonardo's description found in his note book for turbulence is one of the very first descriptions of turbulence, or "turbolenza" as da Vinci named this intricate fluid behaviour

"...thus the water has eddying motions one part of which is due to the principal current, the other to the random and reverse motion. ...the smallest eddies are almost numberless, and large things are rotated only by large eddies and not by small ones and small things are turned by small eddies and large" (Richter et. al 1970)



Figure 2.2: Eddying motion in water sketched by Leonardo da Vinci in ca 1508-1513. Royal Collection Trust/ © Her Majesty Queen Elizabeth II 2016.

In the turbulent flow eddies move around, undergo stretching and twisting and exchange energy and momentum, while interacting nonlinearly with each other. The largest eddies, associated with the low frequency fluctuations extract their energy from the mean flow. As these eddies undergo vortex stretching, smaller and smaller eddies of higher frequency levels, with shorter and shorter eddy turnover times are generated. Thus, the energy flows from the largest scales via the hierarchy of eddies to the smallest scales. This process is called turbulent energy cascade, which is sometimes referred to as Richardson cascade according to Lewis Fry Richardson, who first introduced the idea in 1992:

“We realize thus that: big whirls have little whirls that feed on their velocity, and little whirls have lesser whirls and so on to viscosity” (Richardson 1992)

At the smallest scales, the kinetic energy of the flow is dissipated into internal energy through the work of flow against the viscous stresses. Due to the highly dissipative nature of turbulence, to maintain it, a source of energy is needed at the large scale. This cascade of energy is sketched in Fig. 2.3. (Frisch 1995, Tennekes and Lumley 1972)

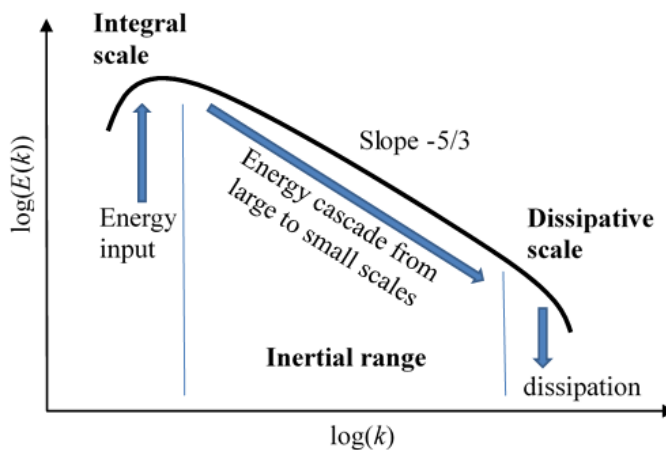


Figure 2.3: Schematic picture of turbulent energy cascade.

2.1.3 Turbulence as a dynamical system

The papers of Andrei Nikolaevich Kolmogorov published in 1941 (Kolmogorov, 1941 a-c) are considered to be the basis of the present understanding of high Reynolds number turbulence as a dynamical system (Frisch, 1995). They present a viewpoint for the determination of kinetic energy transfer across the whole range of scales up to the dissipative end of the spectrum. Eddies at large scales, called integral length scales (labelled with l_1) have the length of the flow boundaries. The Reynolds number of these scales is in the order of the flow. Accordingly, viscosity is insignificant and no dissipation takes place on these large scales. Consequently, their energy is transferred to smaller

scales, where the viscosity becomes dominant resulting energy dissipation. In small length scales (high frequency scales) eddies become homogenous and isotropic. They are independent of large scale motion. The first Kolmogorov similarity hypothesis (Kolmogorov, 1941a) states, that the small scales have a universal form. The smallest dissipative scales are determined simply by two governing parameters, the fluid kinematic viscosity ν and turbulent energy dissipation rate ε . The smallest dissipative scale of turbulence, called Kolmogorov length scale, is defined as

$$l_K = (\nu^3/\varepsilon)^{1/4}. \quad (2.2)$$

Kolmogorov's second similarity hypothesis (Kolmogorov, 1941a) concerns the scales l in a range much smaller than the energy containing scales at which turbulence is generated and much larger than the Kolmogorov dissipative scales $l_K \ll l \ll l_I$, known as the inertial subrange. According to this hypothesis, in these scales, turbulence statistics are universal and controlled only by the wavenumber $k=l^{-1}$, and dissipation rate ε . These hypotheses lead to the famous $-5/3$ law of Kolmogorov which states that at the inertial subrange, energy spectrum of turbulence is a function of wavenumber as

$$E(k) \sim \varepsilon^{2/3} k^{-5/3}. \quad (2.3)$$

This $k^{-5/3}$ law is supported by experimental and numerical data. (Frisch, 1995; Jiménez, 2004)

Kolmogorov's theory has also its deficiency as it assumes scale-invariant statistics in the inertial range. This self-similarity of the energy cascade is not supported by experiments. Scaling can be studied via the structure functions $S_p(\mathbf{r})$ of the velocity increments $\delta_r u = u(\mathbf{x}+\mathbf{r})-u(\mathbf{x})$ at scale r in the inertial range as

$$S_p(\mathbf{r}) = \langle |\delta_r u|^p \rangle \sim r^{\zeta(p)}, \quad (2.4)$$

where \mathbf{x} is the position, \mathbf{r} is the space vector, u is the component of the velocity in the direction of \mathbf{r} , $\zeta(p)$ is the scaling exponent and the angular brackets denote time averaging. Kolmogorov's scale similarity assumption leads to the prediction

$$\langle |\delta_r u|^p \rangle \sim (\varepsilon r)^{\zeta(p)}, \quad (2.5)$$

where the scaling exponent takes the value $\zeta(p) = p/3$. This statistical theory of turbulence by Kolmogorov is often referred as K41. However, experimental values of scaling exponents diverge from the linear K41 prediction $p/3$ (Benzi et al. 1993, Eyink 2008). With increasing the order p , the scaling exponents become noticeably lower than K41 prediction, showing the non-linear behaviour. This anomalous scaling indicates that the energy cascade from large to small scales is strongly intermittent inconsistent with the Kolmogorov's self-similarity assumption. In dynamical systems, intermittency can be observed as calm periods that are interrupted by singular events (bursts) that occur chaotically. (Frisch 1995, Jiménez 2004)

The urge to gain fundamental understanding of the intermittent energy cascade from large scale eddy structures to the small-scale eddies in turbulent field motivated the development of shell models, which are a class of dynamical deterministic models (Biferale 2003). Origin of shell model study goes back to the 1970's, when Lorenz (1972), Siggia (1978) and Russian school (Desnyansky and Novikov 1974, Gledzer 1973) started the study of these fascinating models. The shell models are capable of depicting the phenomenon of high Re turbulent energy cascade with a moderate computational cost by considering a discrete set of wave vectors, a shell, in Fourier space and describing the evolution of the shell variables by a coupled set of nonlinear ordinary differential equations. These shells can be thought of as counterparts of eddies, as the energy is injected at large scale shells, transformed through different scale shells and finally dissipated at the smallest scale shells. Interest on shell models was raised, when another outstanding feature was found, namely the displaying of the energy cascade intermittency with scaling exponents deviating from Kolmogorov's non-intermittent prediction (Pouquet et al. 1984, Ohkitani and Yamada 1989, Jensen et al. 1991). These models, that are developed to mimic the Navier-Stokes equations, were considered to yield a meticulous description of turbulent phenomenon, with less computational effort compared to numerical simulations of full Navier-Stokes equations, even in case of high Re . These models are of our interest in this research work.

2.1.4 Turbulence modelling

It is commonly agreed that theoretical description of turbulence is covered by Navier-Stokes (NS) equations, developed by Claude-Louis Navier and Gabriel Stokes in 19th century. The NS equations are partial differential equations, whose nonlinearity and strong dependency from initial and boundary conditions make them extremely challenging or impossible to find exact solutions for all the wide ranging turbulent length scales. Analytical solutions to NS equations are practically excluded because of all the complexities, so the possible ways to utilize them for turbulence study are through simulation and approximation.

Direct numerical simulation (DNS) is fully deterministic approach for turbulence, where the time-dependent NS equations are numerically solved for the spectrum of energy scales from container scale to the tiny dissipative eddies scales. As the number of scales to be resolved increases with the Reynolds number, DNS becomes computationally very costly requiring large number of grid points and very short time scale. So, the DNS method is reasonably usable only for cases with low Re and simple flow configurations. It is also a useful tool in the development of other methods for the treatment of turbulence in real physical applications.

Fully statistical methods are often used for engineering purposes. These methods seek the statistical evolution of the flow and require fluctuations modelling. One such approach is Reynolds-averaged Navier-Stokes (RANS) equations (Reynolds 1895), in which only the time-average of the flow equations is solved and modelling is needed to deal with the fluctuation part. Examples of modelling approaches for RANS are zero-equation models,

like Boussinesq eddy-viscosity approximation (Boussinesq 1877) and Prandtl's mixing-length hypothesis (Prandtl 1925), two-equation models $K-\varepsilon$ (Launder and Spalding 1972) and $K-\omega$ (Kolmogorov 1942) and Reynolds stress equation model (Chou 1945, Rotta 1951). Such models are commonly in use for many industrial flow applications and a lot of work is acquired constantly to find the model parameters for the new complex flow geometries.

Semi-deterministic methods for turbulent flows are useful, when there is a need for resolving the time-dependency of the flow field with less computational resources than DNS. One such unsteady simulation method is Large Eddy Simulation (LES) (Smagorinsky 1963), where large energy-containing scales are computed and the influence of the smaller scales is covered by subgrid-scale models. For high Reynolds number flows this is still computationally quite demanding and other methods have been developed, which can be seen as mixtures of LES and RANS, like Detached Eddy Simulation (DES) (Spalart et al. 1997), Unsteady RANS (URANS) and Hybrid LES-RANS.

Dynamical systems approach offers another point of view in turbulence study. Shell models (Bohr et al. 1998, Biferale 2003) are such dynamical systems, that introduce a simpler way to capture the fundamental mechanism of the turbulent energy cascade, with the intermittent scaling exponents. They are constructed to imitate the full Navier-Stokes equations in Fourier space and are capable of catching the phenomenon of turbulence by a limited number of ordinary differential equations (ODEs). The advantage of shell models is the reasonable number of degrees of freedom at high Reynolds numbers, growing only logarithmically with Re , whereas for DNS it is $Re^{9/4}$. Shell models are useful tool for the study of energy cascade time properties, but turbulence is also a phenomenon of many spatial scales. For that reason, a spatio-temporal shell model in one space dimension, was introduced by Benzi et al. (1996). This model is the one that is modified here for the insertion of dispersed phase particle in turbulent field.

2.1.5 Turbulent modulation in dispersed phase two phase flow

If the modelling of single phase turbulent flows is challenging, even more complexity is added with the second phase. Our interest is in turbulent dispersed phase two phase flows, where the second (dispersed) phase (particles, drops or bubbles, hereafter called particles) is distributed within the continuous carrier phase. The turbulent dispersed-phase multiphase research field is broad and active with numerous experimental and numerical studies (Poelma and Ooms 2006, Balachandar and Eaton 2010, Saber et al. 2015, Hoque et al. 2016, Michaelides et al. 2017). The major challenge for modelling these flows arises from the particle-turbulence interaction, which is still lacking fundamental detailed understanding needed for the prediction of dispersed phase multiphase flows.

The most common treatment for the dispersed-phase is the point-particle approach (Sundaram and Collins 1999, Naso and Prosperetti 2010, Kuerten 2016). However, point-particle DNS is applicable only to small particle cases with diameter smaller than

Kolmogorov length scale of the flow (Hwang and Eaton 2006). In many practical particulate multiphase applications, like fluidized beds or solid transport, the particles are larger and the effect of finite particle size cannot be ignored. Thus, other methods are needed to handle the particle-fluid interaction (Volk et al. 2008). The modelling challenge is produced by the multiscale nature of the problem, and more challenge is added with increasing turbulence Reynolds number. The DNS techniques, which are developed for solving the flow field around each of the individual particles, are computationally expensive, (Balachandar and Eaton 2010, Bourgoin and Xu 2014). So, there is a need for better understanding of the turbulence modification produced by the particles in order to improve the handling of the dispersed phase and increase the efficiency of dispersed-phase multiphase turbulence modelling.

One of the main effects of the particles on the turbulence is the enhanced energy dissipation rate around the particles (Saber et al. 2015). The aim of our research lies in this aspect of turbulence modulation. Despite the broad research interest on turbulent dispersed-phase multiphase flows, only a few studies report the local dissipation effects around finite-size particles located in turbulent flow field in specific cases. The physical picture of the particle influence on the carrier fluid in two phase flows is reviewed through some experimental and numerical studies summarized in Table 2.1. Experimental studies have been carried out by Tanaka and Eaton (2010) and Hoque et al. (2016). Tanaka and Eaton (2010) examined the turbulence modification in case of 500 μm glass, 250 μm glass and 250 μm polystyrene particles, which means about 4 and 2 times the Kolmogorov length scale l_K , located in stationary isotropic turbulence. Taylor microscale Reynolds number Re_λ was 127 for the unladen case. Highly elevated dissipation was discovered around particle, which was about three times the unladen case dissipation. Hoque et al. (2016) used an oscillating grid turbulence apparatus to study the turbulence modulation in the presence of single glass particles of diameters 1-8mm, which means about 10 to 77 times the Kolmogorov length scale l_K , when Taylor Reynolds number was 12-64. Energy dissipation rate was found to increase, as particle size was enlarged and it was found to be higher in the direct vicinity of particle surface reducing further away from particle. More than 70% increase in energy dissipation rate was found in the presence of particles, compared to the unladen case, for the larger particles (3-8mm). Also, an enhancement of dissipation rate in the presence of smaller (1mm) particles was observed for larger Reynolds numbers. Numerical simulation techniques have been used by Burton and Eaton (2005), Lucci et al. (2010), Naso and Prosperetti (2010), Cisse et al. (2013), Wang et al. (2014) and Brändle de Motta (2016), as described in Table 1. Burton and Eaton studied a single particle of size $2l_K$ in decaying turbulence, with particle Reynolds number Re_P approximately 20 and found 20% higher dissipation rate around particle inside 1.5 particle diameter d_P compared to the unladen dissipation. Lucci et al. studied moving solid particles ($d_P=16l_K \dots 35l_K$) in decaying turbulence with $Re_P=10$ and found the dissipation rate was elevated close to the particle surface, which was larger at the front of the moving particle. Naso and Prosperetti (2010) studied single fixed particle ($d_P=8l_K$) in forced turbulence ($Re_P=20$) and detected enhanced mean dissipation rate in the direct vicinity of the particle, compared to the single-phase flow simulation. Cisse et al. (2013) used DNS to study large spherical particles of sizes $d_P=17l_K$, $34l_K$ and $67l_K$ in developed

homogeneous turbulence ($Re_\lambda=160$) and found an increased average dissipation rate around particle. For the case of $d_p=34l_K$ it was over 2,5 times the mean kinetic energy dissipation rate within the range of d_p from the particle surface. Wang et al. (2014) investigated solid free particles of size $d_p=8l_K$ in forced turbulence ($Re_p=6\dots10$) with DNS technique in Lattice-Bolzman method. They found the dissipation rate enhancement in the vicinity of particle to be 6 times larger than the mean dissipation rate.

These experimental and numerical simulation studies (Table 2.1) show when finite size particles are placed in turbulent field, the turbulent energy dissipation rate is enhanced in the direct vicinity of the particle or particles inside roughly $1-1.5d_p$ from the particle surface, with the amount of the enhancement varying from 20% higher to 6 times the reference dissipation rate of unladen case or the mean overall dissipation, depending on the case configuration. One of the studies (Hoque et al. 2016) has reported also particle size as effective factor for the amount of increase of the dissipation rate. Obviously, the Reynolds number has its effect on the turbulent energy dissipation. The fact is that, as the Reynolds number is increased, the DNS techniques need a very fine grid and a very small time step, making them computationally extremely costly. Shell models can handle high Reynolds numbers. They are constructed to mimic the real Navier-Stokes equations and share many features with real turbulence. However, they are not direct truncation of NS-equations and cannot be considered as direct description for the real physical situation. Thus, it is complicated to compare a stationary particle implemented in shell model with real moving solid particles in real fluids. Our motivation for this research is to see the impact of the solid obstacle on the distribution of the energy dissipation in these common dynamical models. This is the first time such a solid defect is introduced to the shell models to see the effects of particle on the multi-scale dynamics of the turbulent energy transfer.

Table 2.1: Previous numerical and experimental work concerning turbulent energy dissipation rate modification in the vicinity of dispersed phase particle.

	d_p/l_K	Re	Case information	Conclusions
Burton and Eaton (2005)	2	$Re_p=20$	DNS. Single particle and decaying homogenous isotropic turbulence.	Dissipation at least 20% higher within $1.5d_p$ from the particle surface compared to the unladen case.
Lucci et al. (2010)	16...35	$Re_p=10$	DNS with an immersed boundary method (IBM). Solid spherical freely moving particles and decaying turbulence.	Increased dissipation rate close to the particle surface, mostly in front of a moving particle.
Naso & Prosperetti (2010)	8	$Re_p=20$	DNS with Physalis algorithm. Single fixed particle and forced turbulence.	Drastically enhanced mean dissipation around the particle within $1.5d_p$ from the surface.
Tanaka and Eaton (2010)	about 2 and 4	$Re_T=17...134$	Experimental study with Particle image velocimetry (PIV). Particles (polystyrene/glass) falling in a turbulence chamber (medium: air).	The energy dissipation rate was increased around the particle about 3 times of the mean dissipation rate of the unladen flow.
Cisse et al. (2013)	17,34 and 67	$Re_T=160$	Pseudo-spectral DNS, with IBM for fully-resolved particles. Spherical particles in developed turbulence.	Average dissipation rate around particle within d_p was about 2.5 times the mean kinetic energy dissipation rate, being slightly larger on front and smaller at rear of the particle.
Wang et al. (2014)	8	$Re_p=6...10$	DNS with Lattice-Boltzmann method. Non-sedimenting solid particles and forced turbulence.	Dissipation rates in the vicinity of particles 6 times larger than the averaged overall dissipation.
Brandle de Motta et al. (2016)	20	$Re_T=73$	Fictitious domain and penalty method based fully resolved particle simulations. Forced turbulence.	Dissipation peak 2.5 times of the average fluid dissipation on the front side of the particle.
Hoque et al. (2016)	10...77	$Re_T=12...64$	Experimental study with PIV of single glass particles in an oscillating grid apparatus.	Dissipation rate was found to increase more than 70% in presence of large particles.

2.2 Shell models of turbulence

2.2.1 GOY shell model

The basic idea behind shell models is to capture the rich and complex behavior of turbulence phenomenon described by the Navier-Stokes equations, through much simpler dynamical system (Bohr et al. 1998, Ditlevsen 2001). The computational benefit is gained by keeping only a few variables per Fourier k -space “shell”, an octave of wave numbers $k_n < |k| < k_{n+1}$, with $k_n = k_0 \lambda^n$, where k_0 is the reference wave number and λ is shell spacing parameter ($\lambda > 1$). The typical choice is $\lambda = 2$. The coupled ordinary differential equations are written for the shell variables u_n , which can be viewed as the velocity increment $|u(x+l) - u(x)|$ on an eddy of length scale $l \sim k_n^{-1}$. Alternatively, it can be interpreted as the characteristic energy of n -th wavenumber shell $|u_n(t)| \sim \sqrt{\int_{k_n}^{k_{n+1}} 2E(k, t) dk}$. The set of shell model equations describes the temporal behavior of the turbulent energy cascade. The evolution equations for the shell variables u_n have the general form as,

$$\frac{\partial u_n}{\partial t} = k_n \sum u_{n'} u_{n''} - \nu k_n^2 u_n + F_n, \quad (2.6)$$

including the nonlinear interaction terms (first term of the right side) as quadratic combinations of $k_n u_{n'} u_{n''}$, typically restricted to the neighbor (n') or next to neighbors (n'') of shell n , the linear term for the velocity, i.e., the dissipation (second term of the right side), where ν is the kinematic viscosity, $\nu \sim 1/Re$, and finally, the forcing F_n , usually acting on the large-scale shells to maintain the turbulence.

Perhaps the most exploited shell model is the GOY shell model (Gledzer 1973, Ohkitani and Yamada 1989). It is also the starting point for the spatio-temporal model used in this work. The GOY model equations, written for one complex shell variable u_n , while conserving the energy $E = \sum_n |u_n|^2 / 2$ are

$$\frac{d}{dt} u_n = ik_n \left(a u_{n+1}^* u_{n+2}^* + \frac{b}{\lambda} u_{n+1}^* u_{n-1}^* + \frac{c}{\lambda^2} u_{n-1}^* u_{n-2}^* \right) - \nu k_n^2 u_n + \delta_{n, n_0} F, \quad (2.7)$$

where $*$ stands for complex conjugate of the complex variable. The parameters a , b , and c are real constants satisfying the relation $a+b+c=0$ and δ_{n, n_0} is the Kronecker delta, which gets value 1 if $n=n_0$ and 0 otherwise. Thus, external force F acts on the largest shell $n_0=1$. A common choice is to rescale time to adjust $a=1$ and define $b=-\beta$ and $c=\beta-1$. Besides energy, another quantity is conserved in inviscid and unforced case, which has the form $\sum_n k_n^{\alpha(\beta, \lambda)} |u_n|^2 / 2$, where $\alpha = -\log_\lambda |\beta - 1|$. Depending on the choice of parameter β , GOY model is said to be of either 2D or 3D turbulence type. For $\beta < 1$ the type is 3D and a common choice for the parameters is $\beta = 1/2$ and $\lambda = 2$ (Kadanoff et al. 1995). Thus, the conserved quantity becomes

$$H = \sum_n (-1)^n k_n |u_n|^2 / 2, \quad (2.8)$$

which can be associated with helicity. 2D type GOY model is achieved with the choice $\beta > 1$. With the conventional option $\beta = 5/4$ and $\lambda = 2$ (Gledzer 1973), the conserved quantity is

$$Z = \sum_n k_n^2 |u_n|^2 / 2, \quad (2.9)$$

which can be interpreted as enstrophy.

2.2.2 Helical shell models

The GOY shell model helicity shares only partial correspondence with the Navier-Stokes helicity. This gave the motivation for the development of helical shell models, which have two complex variables in each shell instead of one, transporting helicity of opposite sign (Biferale and Kerr 1995). In order to get the helical structure of the model closer to the Navier-Stokes helicity, a helical shell model is constructed as generalization of GOY model. The model that is the base of the hierarchical shell model utilized in this work is the helical shell model introduced by Biferale and Kerr (1995) and studied by Benzi et al. (1996), which has the dynamical equations for the shell variables as

$$\dot{u}_n^+ = ik_n (au_{n+1}^+ u_{n+2}^- + bu_{n-1}^+ u_{n+1}^- + cu_{n-2}^- u_{n-1}^-)^* - \nu k_n^2 u_n^+ + \delta_{n,n_0} F^+, \quad (2.10)$$

$$\dot{u}_n^- = ik_n (au_{n+1}^- u_{n+2}^+ + bu_{n-1}^- u_{n+1}^+ + cu_{n-2}^+ u_{n-1}^+)^* - \nu k_n^2 u_n^- + \delta_{n,n_0} F^-, \quad (2.11)$$

where the tree parameters, a , b and c are defined by imposing conservation of energy and helicity, in the inviscid and unforced limit:

$$\frac{dE}{dt} = \frac{d}{dt} \sum_n |u_n^+|^2 + |u_n^-|^2 = 0, \quad (2.12)$$

$$\frac{dH}{dt} = \frac{d}{dt} \sum_n k_n |u_n^+|^2 - |u_n^-|^2 = 0. \quad (2.13)$$

2.2.3 Spatio-temporal tree model

Turbulent flows involve strong intermittent fluctuations in both time and real space. Ordinary shell models have the localization in Fourier space, where real space information is lost. The study of the geometrical effects in turbulent problems with shell models is possible through the development of 0-dimensional shell model, a chain model, to a dynamical tree model with spatial structure. 1-dimensional shell model is obtained by increasing the number of variables per shell with shell index n as 2^n . This is achieved by performing a wavelet-like extension for the single-chain shell model to get a hierarchical energy cascade from large to small scales, in the reminiscent of original Navier-Stokes equations (Nakano 1988, Muzy et al. 1993, O'Neal and Meneveau 1993, Biferale 2003, Benzi et al. 1996). Accordingly, the model can be viewed to describe the evolution of the coefficients of an orthonormal wavelet expansion of a 1D projection of the velocity field as

$$u(x, t) = \sum_{n=1}^N \sum_{j=1}^{2^{n-1}} u_{n,j}(t) \psi_{n,j}(x). \quad (2.14)$$

Discrete translations and dilations are used to create the complete set of wavelets $\psi_{n,j}(x) = 2^{n/2} \psi_{0,0}(2^n x - j)$, where $\psi_{0,0}(x)$ is the mother wavelet. Here, the shell index n defines the scale and index j labels the spatial position on each shell. A schematic of dyadic tree structure in space-scale domain is shown in Fig. 2.4. The total length of the one-dimensional spatial domain is $L_d = 2^{n-1} l_n$, where l_n is the length of one tree segment, named a cell, covering the region $L_j(n)$ in the range of $(j-1)l_n$ to $j l_n$ with the characteristic length $l_n = k_n^{-1}$. Also, as visible in Fig. 2.4, each cell at scale n can be seen as parent for two others at scale $n+1$, which have half the length of that of the parent cell.

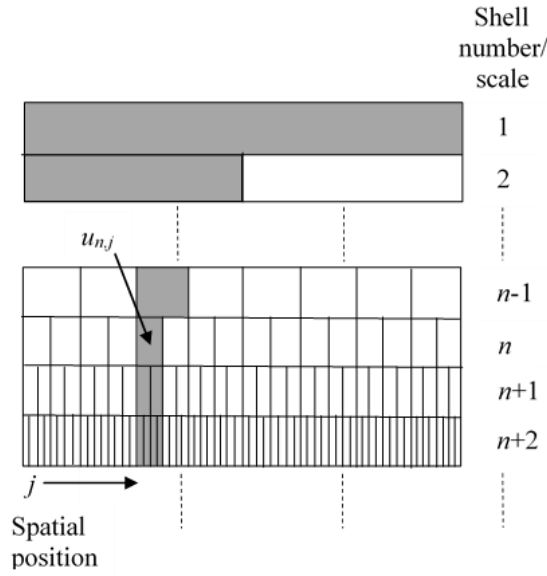


Figure 2.4: The tree model representation of hierarchical structure of turbulent energy cascade.

The dynamical equations for the tree model velocity variable $u_{n,j}$ with helicity considered can be given as

$$\frac{d}{dt} u_{n,j}^+ = ik_n \sum_{n_1, n_2, j_1, j_2} [a_{n_1, n_2, j_1, j_2} u_{n_1, j_1}^{s_1} u_{n_2, j_2}^{s_2}]^* - \nu k_n^2 u_{n,j} + \delta_{n_0, n} F, \quad (2.15)$$

where indices s_1 and s_2 are signs of helicity (\pm) and nonlinear interaction coefficients a_{n_1, n_2, j_1, j_2} are fixed to conserve the energy and the helicity in the inviscid and unforced case (Benzi et al. 1996, Biferale 2003). For $u_{n,j}^-$, the evolution equations are written by reversing the helicities in the above equation. The nonlinear interaction terms are chosen such that locality is considered in both scale and real space domains.

3 Methods

3.1 Theory and formulation

3.1.1 The tree model

In this work, we have utilized the spatiotemporal tree model introduced by Benzi et al. (1997) to study the turbulence modulation triggered by a dispersed particle located in turbulent field. The model originates from the popular GOY shell model (Gledzer 1973, Ohkitani and Yamada 1989). Also, helicity is considered (Biferale and Kerr 1995, Benzi et al. 1996), while transforming a shell model to a hierarchical tree model in one space dimension. A set of complex velocity variables live in the hierarchical tree and interact through the connections between nearby nodes of the tree, which is sketched in Figs. 3.1 and 3.2. The nonlinear interaction terms in the tree model equations are constructed such that each shell variable is allowed to interact with the variables at nearest ($n-1$ or $n+1$) and second-nearest ($n-2$ or $n+2$) scales. In Figs. 3.1(a)-(c) and 3.2(a)-(f) the black node represents the variable $u_{n,j}$, that is connected with solid line to the interacting nodes (variables).

For spatial structure of dynamical interactions, two different models with different structure of interactions are considered as introduced by Benzi et al. (1997), namely model A and model B. In model A, the interactions among cells are vertically organized, meaning that a cell is connected to larger “parenting” cells, and smaller “children” cells (see Fig. 3.1). The corresponding evolution equations for model A are written as

$$\frac{du_{n,j}^+}{dt} = ik_n \left\{ \frac{a}{4} [u_{n+1,2j-1}^+ (u_{n+2,4j-3}^- + u_{n+2,4j-2}^-) + u_{n+1,2j}^+ (u_{n+2,4j-1}^- + u_{n+2,4j}^-)] + \frac{b}{2} [u_{n-1,\bar{j}}^+ (u_{n+1,2j-1}^- + u_{n+1,2j}^-)] + c (u_{n-2,\bar{j}}^- u_{n-1,\bar{j}}^-) \right\}^* - \nu k_n^2 u_{n,j}^+ + \delta_{n,n_0} F^+. \quad (3.1)$$

In model B, local horizontal couplings among cells are also considered, which enables the horizontal transfer of energy between different spatial regions (see Fig. 3.2). The dynamical equations for model B are thus

$$\begin{aligned} \frac{du_{n,j}^+}{dt} = & ik_n \left\{ \frac{a}{4} [(u_{n+1,2j-1}^+ + u_{n+1,2j}^+) (u_{n+2,4j-3}^- + u_{n+2,4j-2}^- + u_{n+2,4j-1}^- + u_{n+2,4j}^-)] + \right. \\ & \frac{b}{2} [u_{n-1,\bar{j}}^+ (u_{n+1,2j-1}^- + u_{n+1,2j}^- + u_{n+1,2\bar{j}-1}^- + u_{n+1,2\bar{j}}^-)] + \\ & c [u_{n-2,\bar{j}}^- (u_{n-1,2\bar{j}-1}^- u_{n-1,2\bar{j}}^-)] + d [-u_{n+1,2j-1}^- u_{n+1,2j}^+ - u_{n+1,2j-1}^+ u_{n+1,2j}^- + \\ & e_1 u_{n,\bar{j}}^- u_{n-1,\bar{j}}^+ + e_2 u_{n,\bar{j}}^- u_{n-1,\bar{j}}^-] + f [u_{n,j+1}^+ u_{n,j+2}^- - u_{n,j-1}^+ u_{n,j+1}^- - u_{n,j-1}^- u_{n,j+1}^+ + \\ & \left. u_{n,j-2}^- u_{n,j-1}^+] \right\}^* - \nu k_n^2 u_{n,j}^+ + \delta_{n,n_0} F^+. \quad (3.2) \end{aligned}$$

Similar sets of equations are constructed for $du_{n,j}^-/dt$ in both models A and B with all helicities reversed in equations 3.1 and 3.2. The indices \bar{j} and $\bar{\bar{j}}$ stand for the integer part

of $(j+1)/2$ and $(j+3)/4$, respectively, and \tilde{j} stands for $(j-1)$ in case of even j and for $(j+1)$ in case of odd j . As an example, in Fig. 3.2(a), the variables interacting with $u_{n,j}$ are $u_{n,\tilde{j}}$ and $u_{n-1,\tilde{j}}$. Horizontal couplings in model B, visualized in Fig. 3.2(f) (variables $u_{n,j-2}$, $u_{n,j-1}$, $u_{n,j+1}$, and $u_{n,j+2}$ interacting with $u_{n,j}$), are treated with periodic boundary condition in spatial dimension by connecting the first position j on each scale to the last one on the same scale.

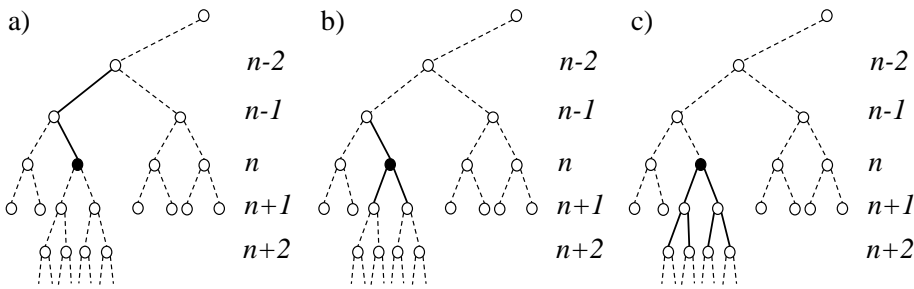


Figure 3.1: The tree presentation of the nonlinear interactions in model A.

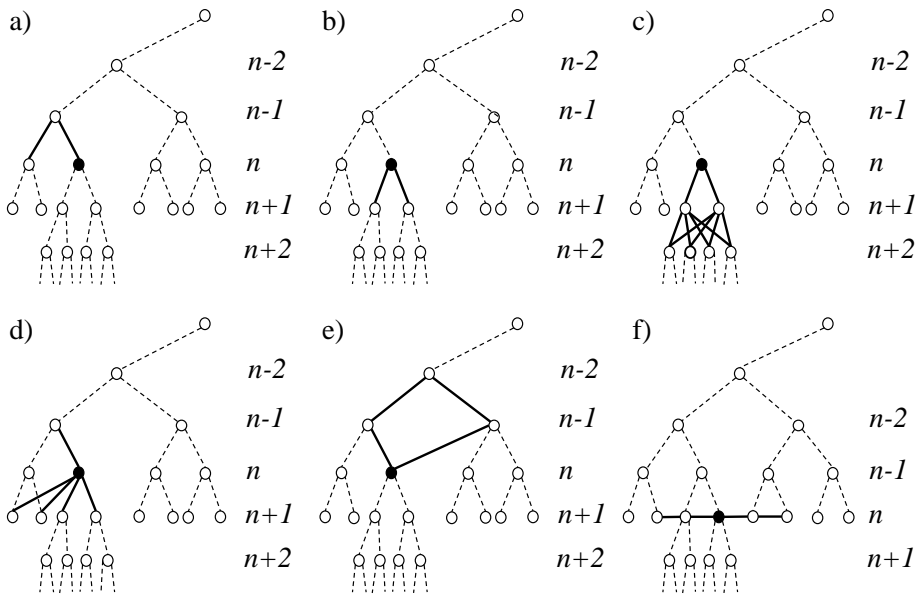


Figure 3.2: The tree presentation of the nonlinear interactions in model B.

Coefficients for interaction terms in Equations 3.1 and 3.2 are chosen to conserve the total energy and helicity

$$dE/dt = d/dt \left(\sum_{n,j} 2^{-n} \left(|u_{n,j}^+|^2 + |u_{n,j}^-|^2 \right) \right) = 0, \quad (3.3)$$

$$dH/dt = d/dt \left(\sum_{n,j} 2^{-n} k_n \left(|u_{n,j}^+|^2 - |u_{n,j}^-|^2 \right) \right) = 0, \quad (3.4)$$

in the inviscid and unforced limit and set to $a=1$, $b=-5/12$, $c=-1/24$, $d=f=1$, $e_1=3/4$, and $e_2=1/4$.

Figure 3.3 illustrates an example of time evolution of the absolute value of velocity $u_{n,j,abs} = \left(|u_{n,j}^+|^2 + |u_{n,j}^-|^2 \right)^{1/2}$ generated by model A for cells located beside the centerline of the hierarchical model domain on the left indexed with $j=J$ on each scale $n=1..N$. This figure visualizes how the highest frequencies associated with $u_{n,j}$ occur in small scale shells (higher wave numbers) while the lowest frequencies are found in larger-scale shells (lower wave numbers). Also, the absolute values of $u_{n,j}$ become higher at larger scales. A disturbance in time series of $u_{n,j}$ travels through the shells starting from the large-scale shells ending up to the small-scale shells via a chain reaction.

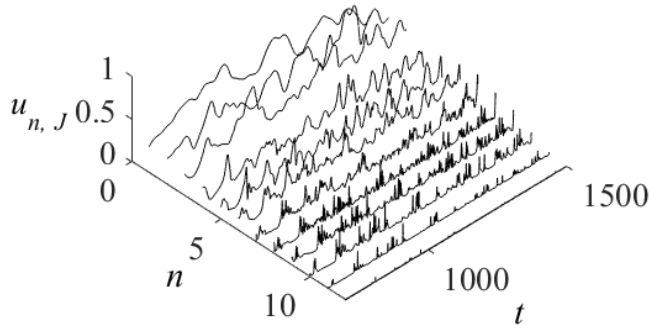


Figure 3.3: A sample of time evolution for the absolute value of velocity $u_{n,j}$ in the cells $j=J$, next to the centerline at the left in the hierarchical domain for each shell produced by model A in unladen flow configuration.

3.1.2 Energy dissipation

In hierarchical shell models, the turbulent kinetic energy is injected at large scales by external forcing and cascaded locally through the cells from large scale shells (small wavenumbers) to the small-scale shells (large wavenumbers), where it is dissipated. The energy dissipation quantities considered here are the energy dissipation density in each cell $\eta_{n,j}$, the total energy dissipation rate ε and the spatially resolved energy dissipation field $\varepsilon_{N,j}$ for the last level sites ($n=N$). The time evolution of energy dissipation rate in

each cell, labeled by the shell number n and the spatial index j and covering the spatial region l_n , is defined as (Benzi et al. 1997)

$$\eta_{n,j} = \nu k_n^2 \left(\left| u_{n,j}^+ \right|^2 + \left| u_{n,j}^- \right|^2 \right). \quad (3.5)$$

The total energy dissipation rate ε is obtained by adding up these cell dissipations $\eta_{n,j}$ over the entire domain including all scales n and spatial positions j as (Benzi et al. 1997)

$$\varepsilon = \sum_{n,j} l_n \eta_{n,j} = \sum_{n,j} k_0^{-1} 2^{-n} \eta_{n,j}. \quad (3.6)$$

The spatial aspects of the model can be viewed through the spatially resolved energy dissipation rate field as (Benzi et al. 1997)

$$\varepsilon_{n,j} = \eta_{n,j} + \sum_{m < n} \eta_{m,k(m)} + \sum_{m > n} \langle \eta_{m,k(m)} \rangle_{I(m)}. \quad (3.7)$$

Figure 2.4 shows with the shadowed boxes the bandwidth of cells that are considered in the spatially resolved energy dissipation rate $\varepsilon_{n,j}$. It considers the energy dissipation contributions living on the smaller and larger scale structures in addition to the cell n,j itself. In the second term on the right side of the equation 3.7, larger scale structures ($m < n$), that contain cell n,j , are considered through index $k(m)$. The third term takes into account the smaller scale structures ($m > n$), that cell n,j covers by averaging them over $I(m)$, which includes the set of structures at certain scale (two cells at scale $n+1$, four at scale $n+2$ and so forth). The most descriptive spatially resolved energy dissipation field is given for the last level sites $n=N$ as

$$\varepsilon_{N,j} = \sum_{m \leq N} \eta_{m,k(m)}, \quad j=1, \dots, 2^{N-1}. \quad (3.8)$$

The temporal and spatial intermittency produced by the tree model can be observed in the time evolution of the total energy dissipation rate and the spatially resolved energy dissipation rate field for $n=N$, respectively. Figure 3.4 shows samples of time evolution of the total energy dissipation rate ε generated by models A and B in case of unladen and particle-laden simulations for $Re \sim 1/\nu = 10^4$. It should be remarked that the Reynolds number is given as $1/\nu$, due to the lack of physical parameters in the shell models. Spatial intermittency produced by the tree model can be observed in the time evolution of the total energy dissipation rate and the spatially resolved energy dissipation rate field for $n=N$. In Figs. 3.5(a)-(b) the spatially resolved energy dissipation rate field $\varepsilon_{N,j}$ is shown at one arbitrary time instant for unladen and laden simulations produced by model A. Figs. 3.5(c)-(d) show the energy dissipation rates $\eta_{n,j}$ of each cell in the entire hierarchical domain at the same instant in Figs. 3.5(a)-(b), respectively. As visualized in Figs. 3.5(c)-(d), the dissipation appears mostly on small scales (the large shell numbers n), as expected. Particle insertion changes the model behavior (particle location is marked with dotted lines in Figs. 3.5(b)-(d)). It is visible that dissipation does not absolutely exist

within the location of particle as the shell variables in that location are zeroed. As time moves on, the configuration of the dissipation field changes and dissipation peaks are observed in different locations. As an example, in Figs. 3.6(a)-(b) the time evolution of the spatially resolved energy dissipation rate $\epsilon_{N,j}$ is shown for one space location in unladen and laden cases, respectively, where the space location is chosen adjacent to particle surface in the laden case. On the other hand, in Figs. 3.7(a)-(b) time evolutions of the dissipation rate $\eta_{n,j}$ are demonstrated at the cells on different scales n , covering one spatial location for unladen and laden case of model A. Again, the spatial location is chosen to be adjacent to the particle surface in laden case. In Figs. 3.7(a)-(b) it can be observed, that dissipation occurs at scales $n=6\dots 12$, where $n=12$ is the Kolmogorov length scale.

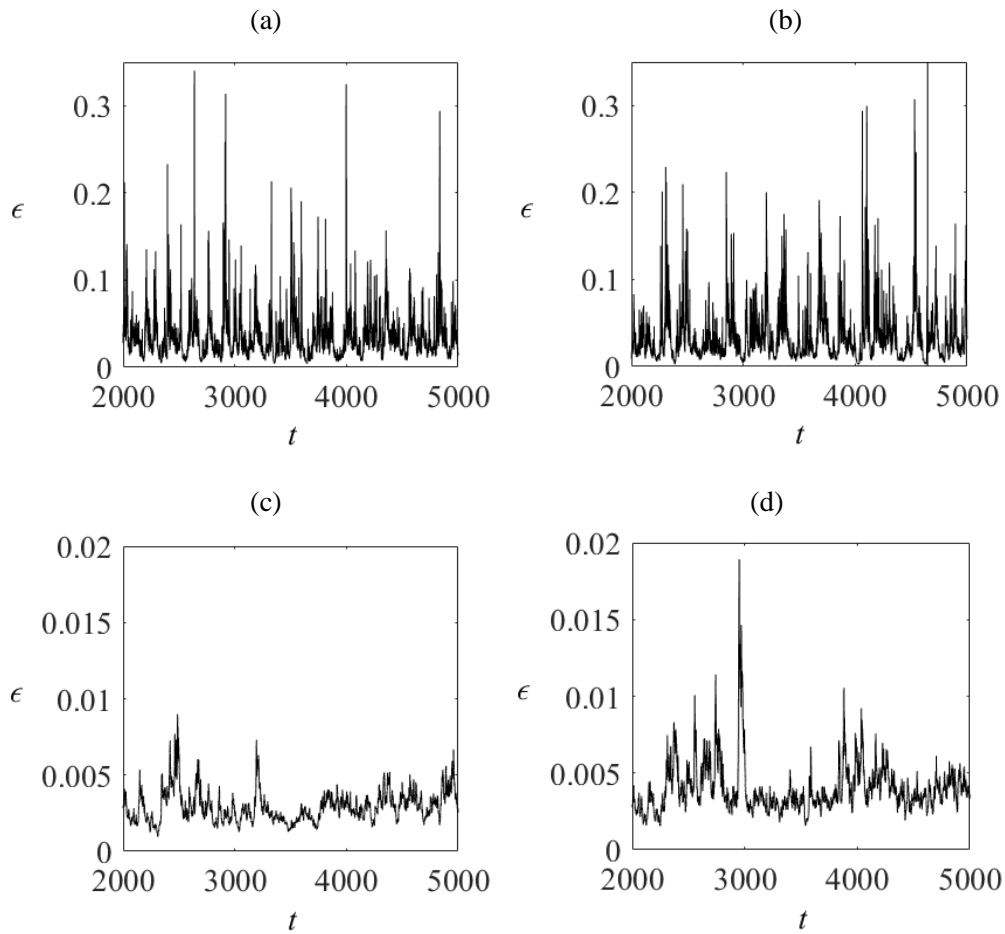


Figure 3.4: A sample of time series of the total energy dissipation rate of (a) unladen case produced by model A, $Re \sim 1/\nu = 10^4$, (b) laden case produced by model A, $Re \sim 1/\nu = 10^4$, particle on scale $n=7$, (c) unladen case produced by model B, $Re \sim 1/\nu = 10^4$, and (d) laden case produced by model B, $Re = 10^4$, particle on scale $n=7$.

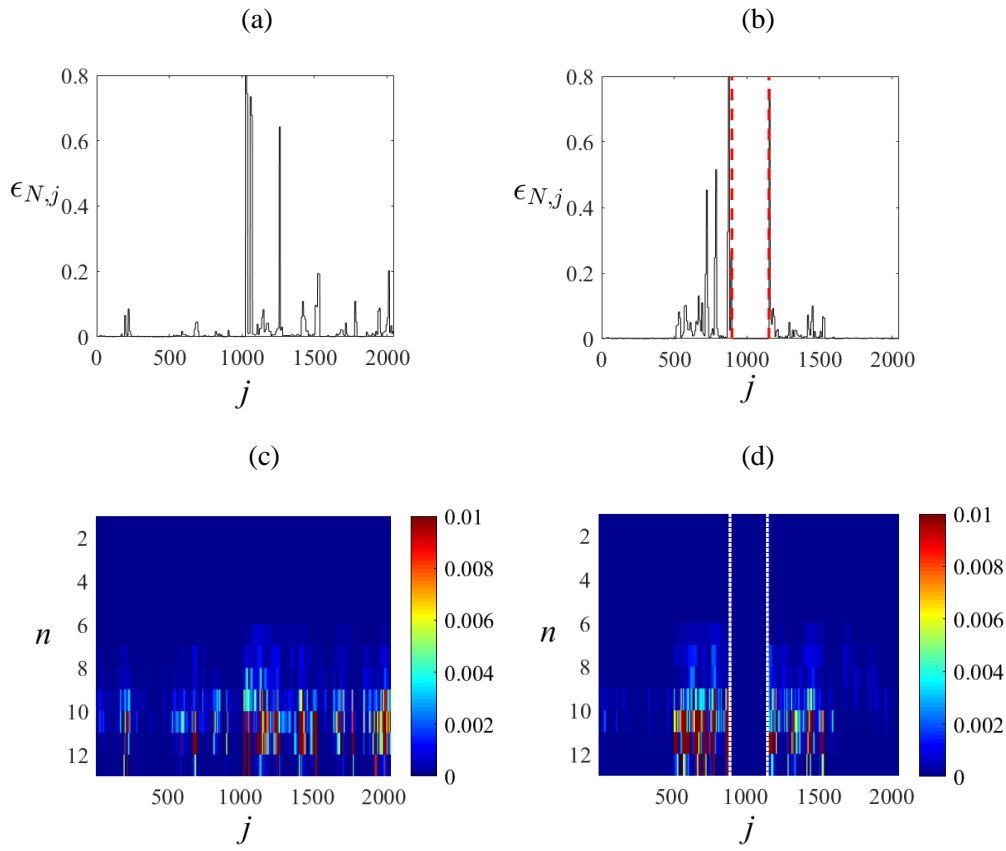


Figure 3.5: Samples of instantaneous configuration of the spatially resolved energy dissipation rate field $\epsilon_{N,j}$ for (a) unladen case, $Re \sim 1/\nu = 10^4$ and (b) laden case, $Re \sim 1/\nu = 10^4$, particle on scale $n=5$ and the entire hierarchical domain of energy dissipation rates in each cell $\eta_{n,j}$ at corresponding time instant for (c) unladen case, $Re \sim 1/\nu = 10^4$ and (d) laden case, $Re \sim 1/\nu = 10^4$, particle on scale $n=5$.

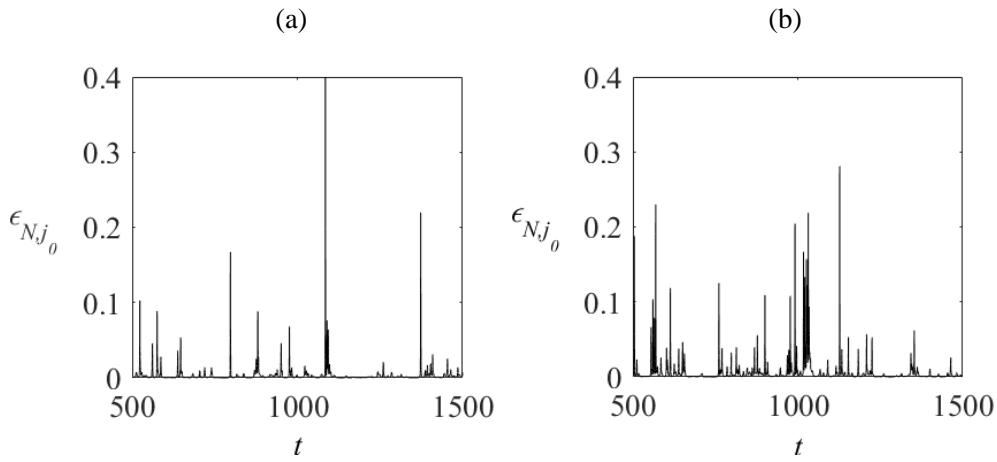


Figure 3.6: Samples of the time evolution of the energy dissipation rate ϵ_{Nj} for one spatial location produced by model A for (a) unladen case, $Re \sim 1/\nu = 10^4$, and (b) particle-laden case, $Re \sim 1/\nu = 10^4$, particle on scale $n=7$, location adjacent to the particle surface.

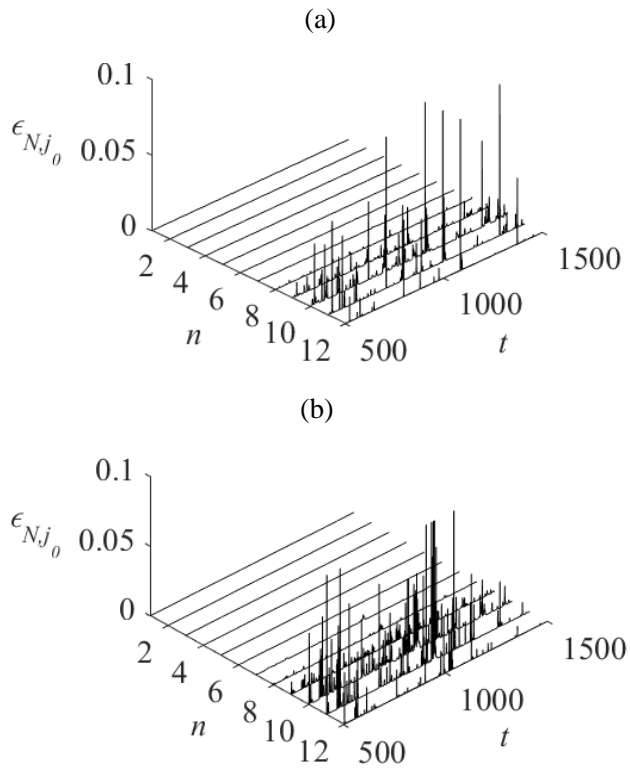


Figure 3.7 Time evolution of the dissipation rate at the cells next to the central line on right at each scale n , produced by model A for (a) unladen case, $Re \sim 1/\nu = 10^4$, and (b) particle laden case, $Re \sim 1/\nu = 10^4$, particle on scale $n=7$.

Through these dissipation quantities introduced in Eqs. 3.5-3.8, and demonstrated through Figs. 3.4-3.7, it is hard to detect and compare the turbulence dissipation modulation produced by insertion of a particle in a turbulent field. Hence, the time average of the spatially resolved energy dissipation field $\bar{\varepsilon}_{N,j}$ is considered, which is illustrated in Figs. 3.8 (a)-(b) for model A and Figs. 3.8(c)-(d) for model B. For the unladen cases (Figs. 3.8(a) and (c)), the time average of spatially resolved energy dissipation rate field $\bar{\varepsilon}_{N,j}$ is roughly constant, but for the laden cases (Figs. 3.8(b) and (d)), the turbulence modulation produced by the particle can be manifested as higher dissipation in the vicinity of particle surface.

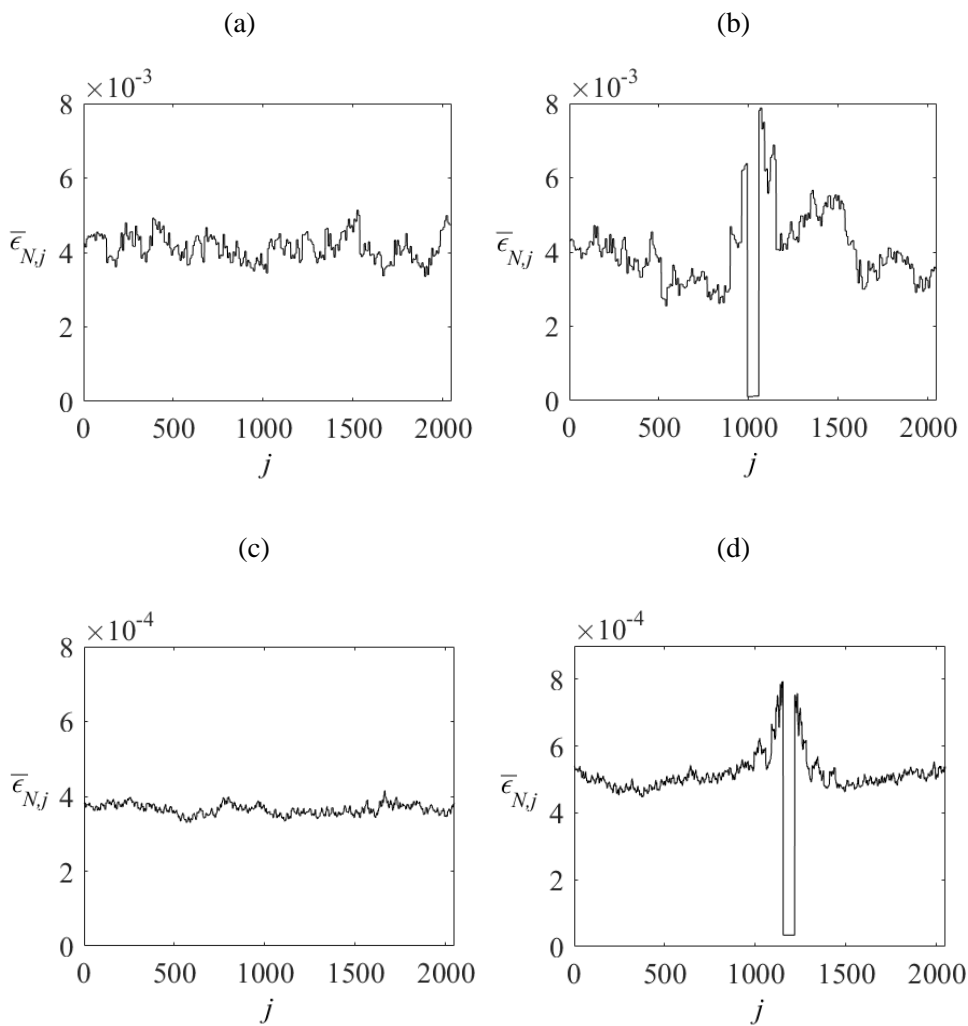


Figure 3.8: The time average of the spatially resolved energy dissipation rate field $\varepsilon_{N,j}$ of (a) unladen case simulation by model A, (b) laden case simulation by model A, (c) unladen case simulation by model B and (d) laden case simulation by model B.

3.1.3 Inclusion of dispersed phase particle into the tree model

The idea of introducing a fixed particle in a hierarchical shell model was first presented by Sikiö and Jalali (2014). Figure 3.9(a) shows a particle located in a turbulent field and Fig. 3.9(b) visualizes how this is implemented in one dimensional hierarchical domain of tree model. Particle size is described by the shell number n and the location by spatial index j , which can have values 1 to 2^{n-1} on each scale n . In the spatial location of particle, the complex helical velocity variables $u_{n,j}^{\pm}$ are zeroed at cell n,j in addition to the cells on the smaller scales on the bandwidth of the particle location, as shown in Fig. 3.9(b) with shadowed boxes. No other modifications have been made for the particle insertion. It should be noted, that in model B, instead of one cell at largest scale n representing the particle, two neighbour cells are set to zero in order to keep symmetry of turbulence around the particle. This is described in more details in Sikiö et al. (2017a). The turbulence modification by a particle is detected as local elevation of the energy dissipation rate in the vicinity of particle as visible in Fig. 3.9(c), which shows the example of time-averaged spatially resolved energy dissipation rate $\bar{\epsilon}_{N,j}$.

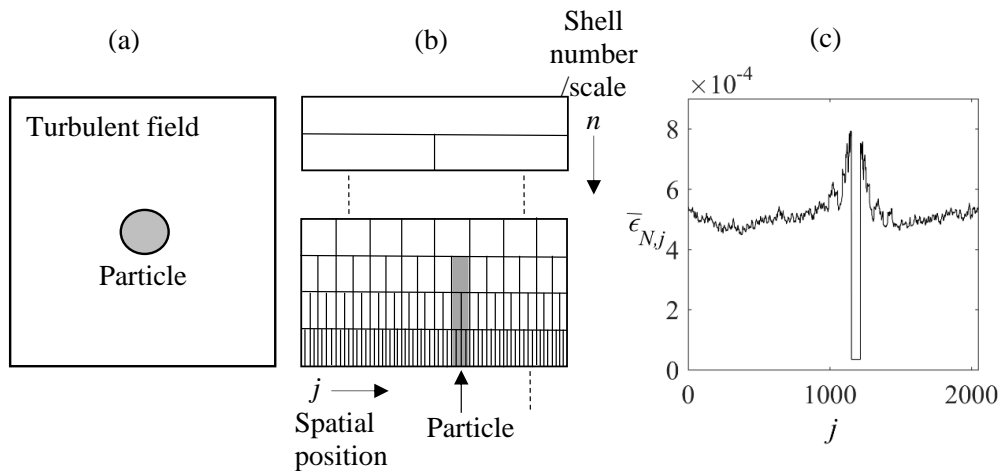


Figure 3.9: (a) A particle placed in a turbulent field. (b) Space-scale representation of hierarchical shell model with a particle represented with zeroed velocities at the cells marked with shadowed boxes at its location. (c) Time-averaged energy dissipation rate ϵ .

3.2 Numerical implementation

The cases studied in this work are listed in Table 3.1 with the parameters used in the simulations. In all studied cases the external forcing is taken to be constant $F^{\pm} = 5.0(1+i)\times 10^{-3}$, shell parameter λ is set to 2 and reference wave number k_0 is 0.0625. The total number of shells N is 12 or 16 depending on the case. Simulation time is given as large-eddy turnover times. The eddy turnover time at shell n is given as

$$\tau_n = (k_n \langle |u_{n,j}| \rangle)^{-1}, \quad (3.9)$$

where brackets are for space and time averaging. In the largest scale n is 1.

Table 3.1: Simulation cases with corresponding variables.

	$1/\nu$	d_P/l_K	d_P/L_d	N	τ_1	
Model A	333	unladen	-	12		(Sikiö and Jalali 2014)
Model A	333	2	1/128	12		(Sikiö and Jalali 2014)
Model A	10^4	unladen	-	12	260	(Sikiö and Jalali 2014)
Model A	10^4	8, 16, 32, 64, 128, 256	1/256, 1/128, 1/64, 1/32, 1/16, 1/8	12	55...280	(Sikiö and Jalali 2014)
Model B	10^4	unladen	-	12	350	(Sikiö et al. 2017a)
Model B	10^4	32, 64, 128	1/64, 1/32, 1/16	12	230...300	(Sikiö et al. 2017a-b)
Model B	10^4	16, 256	1/128, 1/8	12	230...270	(Sikiö et al. 2017b)
Model B	10^4	64 (dual particles)	1/32	12	260...300	(Sikiö et al. 2017a)
Model B	5×10^4	unladen	-	16	160	(Sikiö et al. 2017c)
Model B	5×10^4	256	1/32	16	70	(Sikiö et al. 2017c)
Model B	10^6	unladen	-	16	70	(Sikiö et al. 2017c)
Model B	10^6	64	1/512	16	70	(Sikiö et al. 2017c)

As initial condition for the simulations, the velocity variables $u_{n,j}^\pm$ were given random values. This was necessary for the model A, in absence of horizontal interactions, to see the spatial intermittency in addition to the temporal intermittency, as noted by Sikiö and Jalali (2014). There are two ordinary differential equations (ODEs) for each cell identified by (n, j) , which come from the model equations. The entire set of ODEs is solved in time using Runge-Kutta method available in MATLAB v. R2013b, with tiny time steps controlled by the ode45 solver.

4 Results

4.1 Performance of the tree model

Performance of the shell model A with particle insertion was studied by Sikiö and Jalali (2014) via simulations, which were compared to the fully resolved simulations of particle-turbulence interaction implemented by Burton and Eaton (2005). They studied a fixed particle of the size twice as the Kolmogorov length scale l_K in decaying turbulence. Shell model simulations were performed by Sikiö and Jalali (2014) with parameters matching to the parameters of Burton and Eaton (2005) to test the behaviour of the model with particle insertion. Burton and Eaton found in their simulations a turbulent energy dissipation rate enhancement within the distance of 1.5 times the particle diameter from the particle surface as 20% higher than the unladen case. The shell model simulations using model A showed approximately 7 percent higher dissipation rate in the vicinity of the particle with respect to the unladen simulation. The dissipation rate profiles of the simulations of shell model A (Sikiö and Jalali 2014) are shown in Fig. 4.1. It should be noted that the particle was introduced in the shell model by setting the shell variables to zero within the location of particle at scales of particle size and smaller. If particle size is near the Kolmogorov scale and dissipation occurs also at larger scales than particle size, some lower values of dissipation are detected also in the location of particle. Furthermore, no supplementary source for dissipation at the interface (particle surface) have been introduced. In the shell model, a decay of dissipation rate is observed in the direct vicinity of particle surface and the dissipation peaks are moved further from the particle surface. This can be explained by the synchronization effect (Benzi et al. 1997), which has more influence in model A than in model B due to the lack of horizontal interactions in model A. This appears as synchronized nearby variables, which are covered by fundamentally the same equations. In model A, this synchronization starts from smaller shell numbers than in model B, which also includes horizontal interactions in addition to vertical ones.

Similar simulation configuration was used for testing the performance of shell model B and comparing it to model A (Sikiö et al. 2017a). Here, a larger Reynolds number was used as $Re \sim 1/\nu = 10^4$, in addition to a larger particle with the size of $64l_K$ to avoid the disadvantage caused by synchronization. The time averaged spatially resolved dissipation rate profiles of the simulations are shown in Fig. 4.2. The energy dissipation rate within particle diameter was roughly 3.5 times higher than the unladen case for model A, whereas for model B the dissipation rate was only about 80% higher than that of the unladen case. In simulations of model B, dissipation rate is slightly increased in further locations as well, which is due to the presence of horizontal interactions enabling a wider spatial range of energy exchange among the variables. This also explains the different amount of enhancement of dissipation rate near particle surface in models A and B.

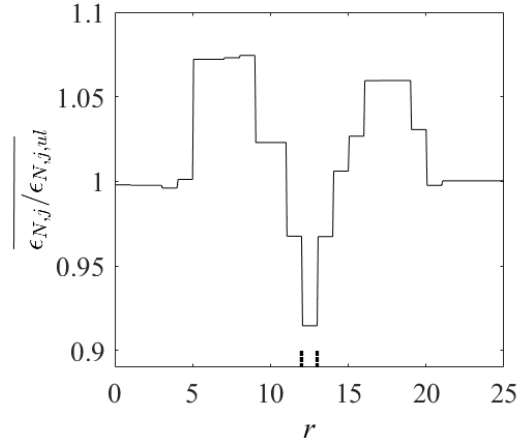


Figure 4.1: Time-averaged ensemble average of turbulent energy dissipation rate profile over 30 cases resulted in the shell model simulations (model A) of particle laden turbulence in (Sikiö and Jalali 2014). The dissipation rate profile is normalized by the unladen case values and the space variable by the particle diameter. Location of particle is marked with dotted lines.

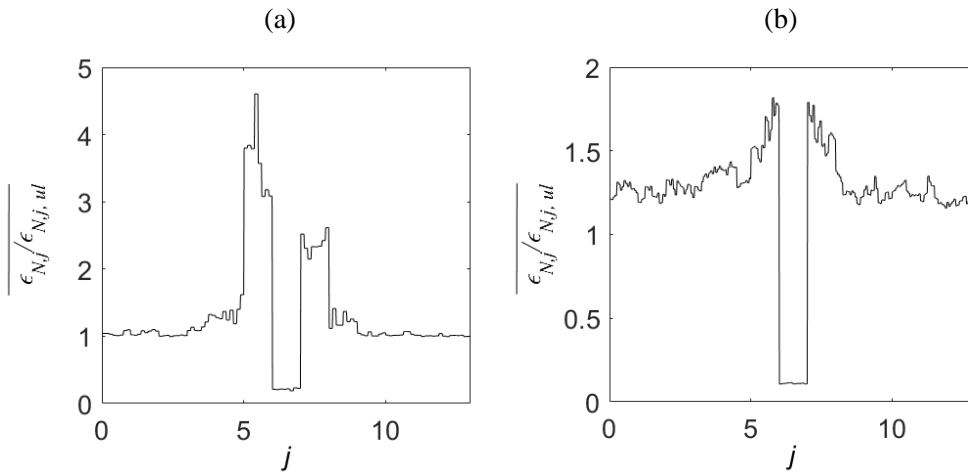


Figure 4.2: Time-averaged ensemble average of turbulent energy dissipation rate profiles over 44 cases performed in (Sikiö et al. 2017a) for: (a) model A, and (b) model B. Space variable is non-dimensionalized by the particle diameter and dissipation rates normalized by the corresponding unladen case values.

Several Computational fluid dynamics (CFD) simulations were performed using the computer package of ANSYS-Fluent for comparison to the tree model simulations. Three different turbulence models were used, including k -epsilon, k -omega and 7-equation Reynolds Stress model. Particle was located in turbulent field at the centre of a cubic box

with one side with velocity inlet condition and its opposite side with pressure outlet condition. The side walls were assigned with symmetry boundary condition. The energy dissipation values were calculated as area-weighted averages over spherical surfaces of the same centre as the particle. In Fig. 4.3, the cases are demonstrated that match with the DNS case of Burton and Eaton (2005). Several mesh sizes were tested from coarser to finer meshes. The mesh size was selected, which did not show the significant changes in the results. The particle Reynolds number is nearly 21 in Fluent simulations, and the size of particle is $d_p/l_K=2.45$ for the case with k -epsilon model, $d_p/l_K=1.46$ for k -omega model and $d_p/l_K=1.4$ for 7-equation Reynolds Stress model. For the comparison, the results of Burton and Eaton (2005) are given in Fig. 4.3 as well. Compared to the results of Burton and Eaton (2005), the Fluent simulations overestimate the dissipation rise, with the closest estimate obtained from k -omega model.

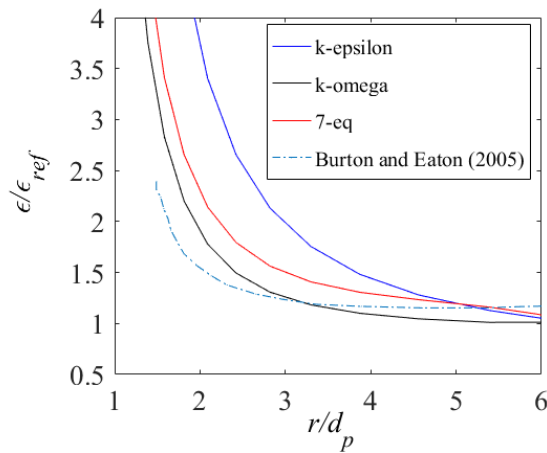


Figure 4.3: CFD simulations of turbulent field with a fixed solid particle using turbulent models k -epsilon (blue solid line), k -omega (black solid line) and 7-equation model (red solid line) by means of ANSYS-Fluent package v. 16.0. For comparison, the results of Burton and Eaton (2005) are given (blue dash-dotted line). ϵ_{ref} is the dissipation of the unladen case for results of Burton and Eaton. For k -epsilon, k -omega and 7-equation models ϵ_{ref} is the dissipation far from the particle surface.

4.2 Scaling properties of the model

The scaling properties of turbulence resulted by the models A and B have been studied via the velocity field structure functions $S_p(n)$, obtained by time and space averaging of the absolute values of the velocity variables over the time period T and space locations j , as given by Benzi et al. (1997)

$$S_p(n) = (T2^n)^{-1} \sum_{t,j} \left(\sqrt{|u_{n,j}^+(t)|^2 + |u_{n,j}^-(t)|^2} \right)^p . \quad (4.1)$$

The moments are expected to follow the scaling law $S_p(n) = k_n^{-\zeta(p)}$ in the inertial range. The scaling exponents $\zeta(p)$ of the velocity structure functions produced by the tree models A and B have been studied by Benzi et al. (1997) and found to be anomalous, i.e. the scaling exponents are found to deviate from the Kolmogorov's prediction $\zeta(p) = p/3$ (Kolmogorov 1941a), revealing intermittency.

The scaling properties of the turbulence produced by the models A and B are investigated in case of different size particles inserted in the model domain (Sikiö and Jalali 2014, Sikiö et al. 2017a). Also, the scaling is examined in case of three different Reynolds numbers. The scaling exponents ζ are obtained by fitting over the inertial range using Extended Self Similarity (ESS): The logarithm of the p th order scaling exponent is plotted against the logarithm of the third order moment $S_3(n)$. The resulting exponents are compared with the Kolmogorov (1941a) non-intermittent prediction $p/3$, often referred as K41, and the theoretical prediction of She and Leveque (1994), which has the form of $\zeta(p) = p/9 + 2[1 - (2/3)]^{p/3}$ and is observed to agree with the experimental results of Benzi et al. (1993) and supercomputer simulation results produced by Fisher et al. (2008).

It should be noted that the existence of interface, like a solid wall, causes perturbations among scales resulting non-homogeneous local effects (Biferale et al. 2003). The local scaling effects are studied in model A and model B by defining the structure functions over the time period T for a location j in space. Three locations are chosen for the study, one near the particle and two farther from the particle surface at different distances.

4.2.1 Unladen and particle laden cases of models A and B

The scaling properties of models A and B with and without particle in the model are considered through velocity structure functions (Sikiö et al. 2017a). An example of finding the scaling exponents ζ of the velocity structure functions is given in Fig. 4.4, which displays the seventh order moment $S_7(n)$ against the logarithm of the third order moment $S_3(n)$ in the unladen and the laden cases of model A and B. Reynolds number is defined as $Re \sim 1/\nu = 10^4$. The anomalous scaling exponents of orders $p=1, \dots, 8$ are visualized in Fig. 4.5, where both unladen and laden simulations have been found in good agreement with the results of Benzi et al. (1997). The comparison with the K41 (Kolmogorov 1941a) non-intermittent prediction and intermittent prediction of She and Leveque (1994) revealed the intermittent characteristics of turbulence generated by the models for both unladen and particle laden cases. The deviation from the linear K41 prediction is observed in higher order scaling exponents with $p \geq 4$. In agreement with the results of Benzi et al. (1997), the model A exhibits more intermittency than model B, which is caused by different interaction range in horizontal (spatial) direction. This was found to be true for the particle laden cases as well. Here, a slight change was found, towards more intermittent regime in particle laden simulations.

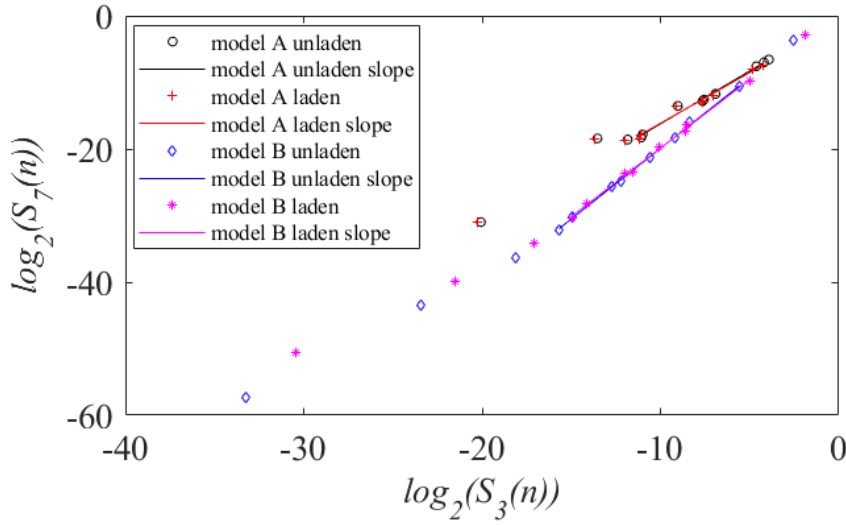


Figure 4.4: The logarithm of seventh order moment $S_7(n)$ against the logarithm of third order moment $S_3(n)$ for model A and B in unladen and laden cases with the particle located at the scale $n=7$ ($d_p/lK=64$ and $d_p/L_d=1/32$).

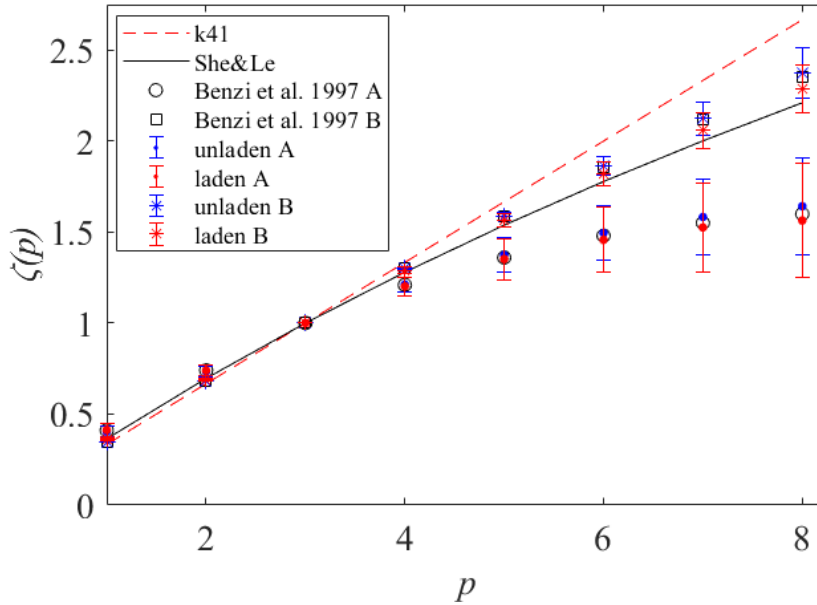


Figure 4.5: The anomalous scaling exponents of orders $p=1, \dots, 8$ for the unladen and laden cases (particle at scale $n=7$) of model A and B. $Re \sim 1/\nu$ is taken as 10^4 in these simulations. Kolmogorov (1994) prediction K41 is given as red dashed straight line, the theoretical prediction of She and Leveque (1994) as black curved line and the unladen simulation results of Benzi et al. (1997) as black circle and square for models A and B, respectively.

The local scaling effects are studied in model A and model B through Figs. 4.6(a) and 4.7(a), respectively. Three spatial locations are considered, which are shown by arrows in Figs. 4.6(b) and 4.7(b) showing the time average of the spatially resolved energy dissipation field. One location is near the particle surface and two locations far from the particle. The scaling exponents are given for comparison in unladen (black square) and corresponding laden case in all spatial locations, as well as the linear prediction of Kolmogorov (1941a) and the She-Leveque prediction (She and Leveque 1994). The anomalous scaling exponents of orders $p=3,\dots,8$ have been shown, which show the deviation from the linear prediction of Kolmogorov (1941a). In model A (Fig. 4.6(a)), the local scaling exponents show an increased intermittency in the nearby location to the particle surface than in the unladen or laden case, when all spatial positions are considered. However, the scaling exponents in locations far from particle show less intermittent behaviour. In model B (Fig. 4.7(a)), minor differences can be observed between scaling exponents in near and far locations to particle surface and all spatial locations. The difference between model A and B, is due to horizontal interactions among shell variables. In model A, the effect of particle is seen right beside the particle owing to the lack of horizontal interactions. In model B, with horizontal interactions activated, the disturbance in one spatial location affects further locations as well.

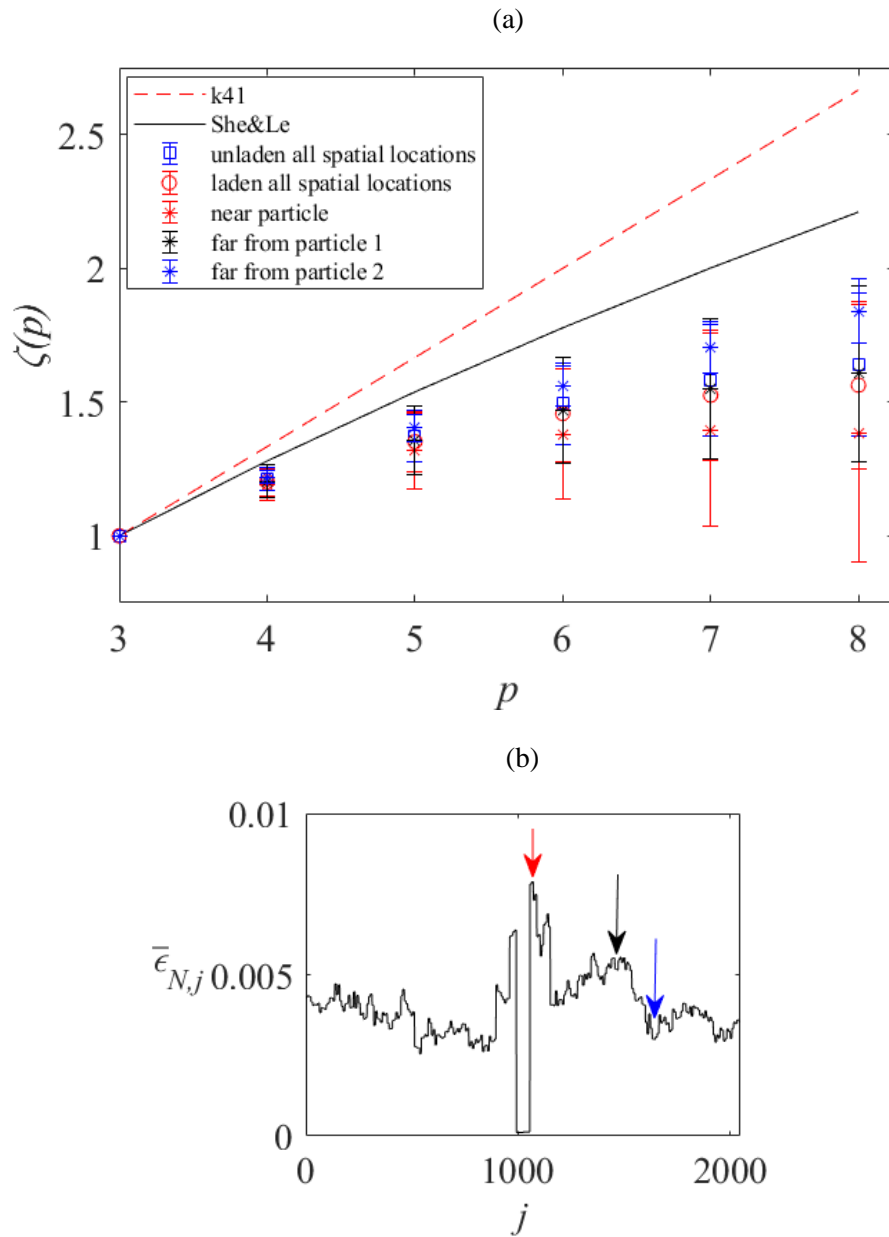


Figure 4.6: (a) The scaling exponents in variable spatial locations in the particle laden simulation with the particle size of $d_p/l_K=64$ in model A (red, black and blue stars). The scaling exponents are shown for comparison in unladen (black square) and corresponding laden case (red circle) in all spatial locations, as well as the linear prediction of Kolmogorov (1941a) (k41, dashed red line) and the prediction of She and Leveque (1994) (She&Le, black curved solid line). (b) The demonstration of selected spatial positions near and far from particle surface in (a) shown by arrow of same colour.

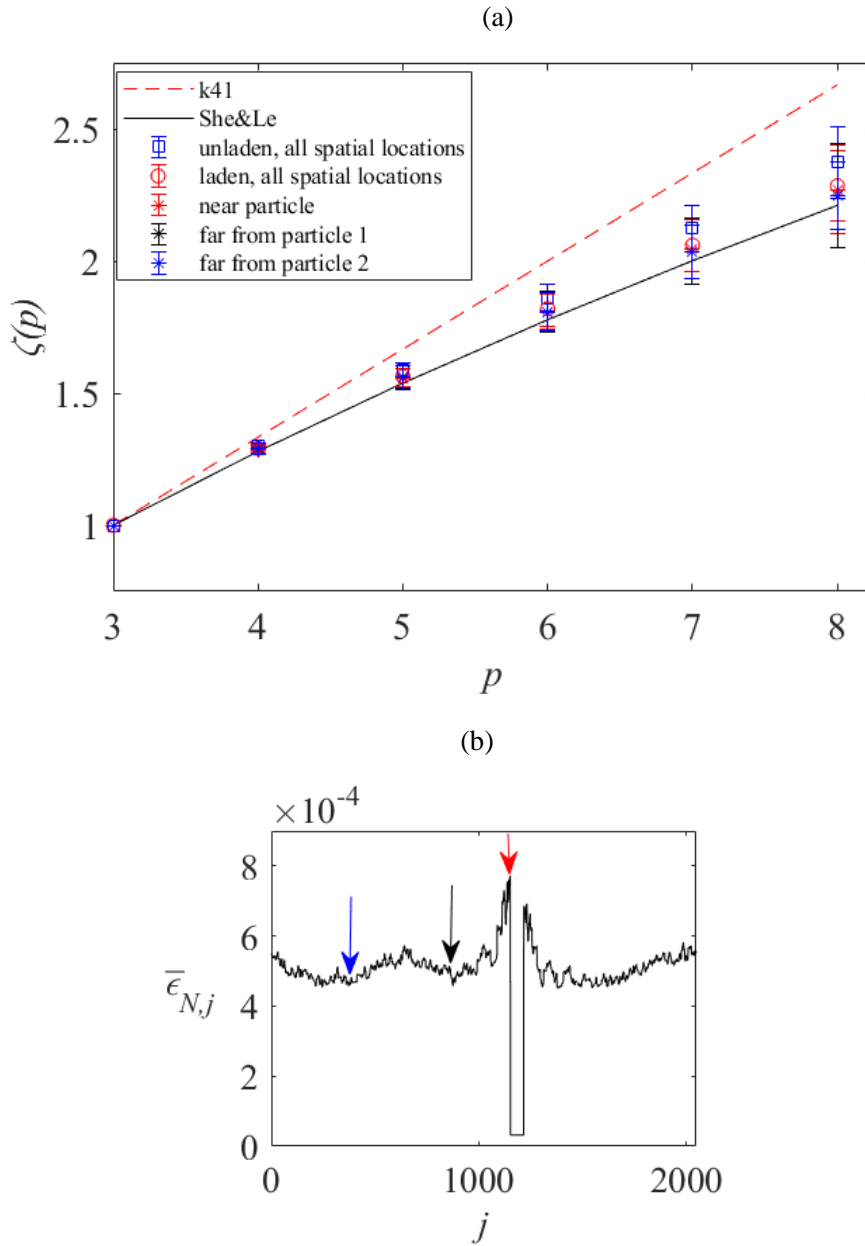


Figure 4.7: (a) The scaling exponents in variable spatial locations in the particle laden simulation with the particle size of $d_P/l_K=64$ in model B (red, black and blue stars). It should be noted that blue stars overlap the black stars. The scaling exponents are shown for comparison in unladen (black square) and corresponding laden case (red circle) in all spatial locations, as well as the linear prediction of Kolmogorov (1941a) (k41, dashed red line) and the prediction of She and Leveque (1994) (She&Le, black curved solid line). (b) The demonstration of selected spatial positions near and far from particle surface in (a) shown by arrow of same colour.

4.2.2 Scaling of the model with different size particles

The scaling of model B is studied in the presence of particle, with variable particle size (Sikiö et al. 2017b). The results are shown in Fig.4.8. Deviation from the linear prediction of Kolmogorov (1941a) is seen in the higher order scaling exponents, which reveals the existence of intermittency. So, the lower order scaling exponents are left out from the figure. The scaling exponents of smaller particle cases show only slight deviation from the corresponding exponents of unladen case. The deviation is larger for the cases with larger particles, towards more intermittent regime.

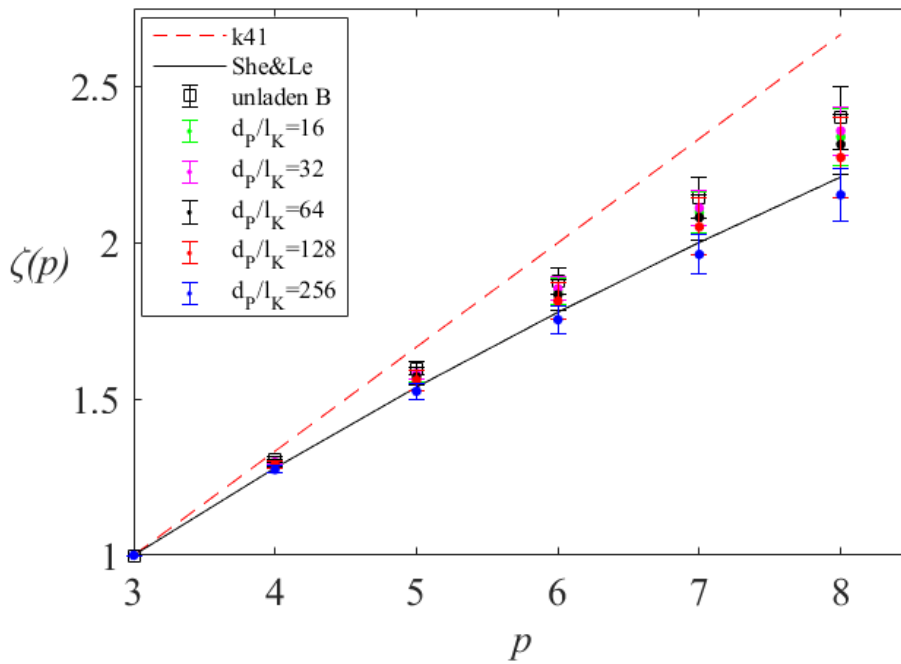


Figure 4.8: The scaling exponents considering all spatial locations for the particle laden simulations with variable particle sizes using model B. The unladen case (black square) and the linear prediction of Kolmogorov (1941a) (k41, dashed red line) and the prediction of She-Leveque (1994) (She&Le, black curved solid line) are given for comparison.

4.2.3 Effect of Reynolds number variation

The scaling properties of the tree model B are studied in the case of higher Reynolds numbers, $Re \sim 1/\nu = 5 \times 10^4$ and $Re \sim 1/\nu = 10^6$, in case of unladen simulation and with particle insertion of particle size d_p as $256l_K$ and $64l_K$, respectively (d_p is $L_d/32$ and $L_d/512$, respectively) (Sikiö et al. 2017c). These are compared to the lower Re case, $Re \sim 1/\nu = 10^4$, with corresponding particle insertions. These cases were studied in (Sikiö et al. 2017a).

The results are shown in Figs. 4.9-4.11. All model cases were found to be intermittent. The deviation from the linear prediction of Kolmogorov (1941a) is seen in higher order scaling exponents ($p > 4$). Fig. 4.9 compares the scaling of unladen cases with different Re . Only very little difference is seen towards higher intermittency along with the decreasing Reynolds number. Also, it should be noted, that the simulation time is shorter for the cases with higher Reynolds numbers, $Re \sim 1/\nu = 5 \times 10^4$ and $Re \sim 1/\nu = 10^6$, than for the lower Re case and this may have some effect on the results.

The trend of increased intermittency due to the particle insertion is seen in Fig. 4.10 for $Re \sim 1/\nu = 10^4$ and $Re \sim 1/\nu = 5 \times 10^4$. Here, the physical size of the inserted particles is the same for both cases. Figure 4.11 shows how the variation of physical particle size in the laden tree model leads to a larger difference in intermittency with respect to the variation of the ratio of particle size to the Kolmogorov length scale. The intermittency is higher for the cases with bigger physical size of particles. For small size particles, like the case with $Re \sim 1/\nu = 10^6$ and particle of size $64l_K$ and physical size of $L_d/512$, the intermittency does not differ from the unladen case, or even decreases slightly.

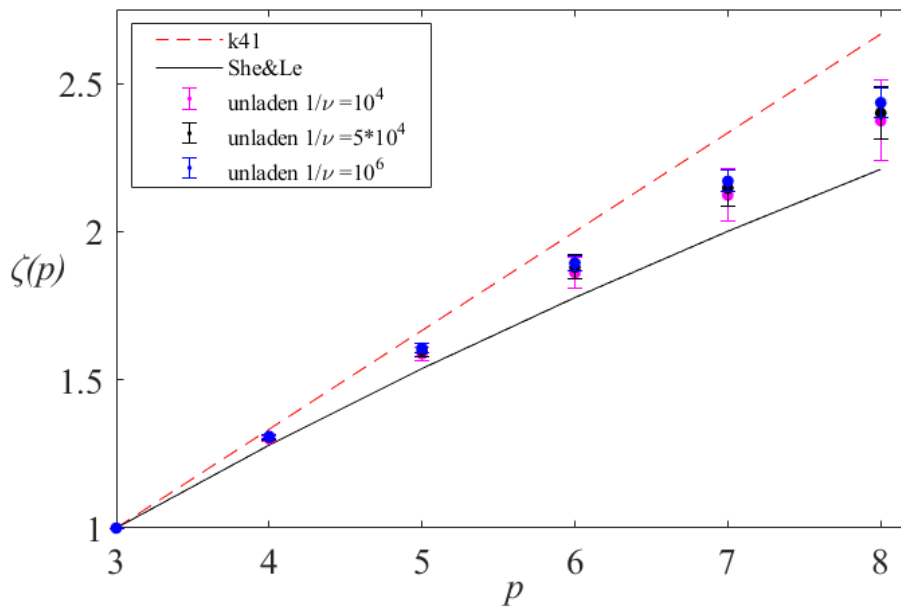


Figure 4.9: Velocity field structure function scaling exponent $\zeta(p)$ for unladen cases with three different Reynolds numbers. For comparison, the non-intermittent prediction of Kolmogorov (1941a) (k41, red dash line) is given as well as the theoretical of She and Leveque (1994).

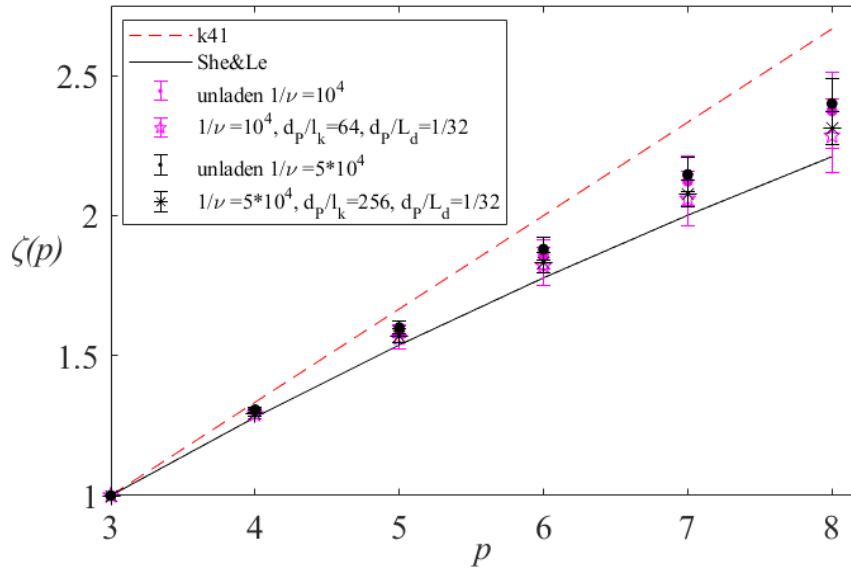


Figure 4.10: Velocity field structure function scaling exponent $\zeta(p)$ for unladen and particle laden cases with two different Re , physical particle size being $L_d/32$ for both cases. For comparison, the non-intermittent prediction of Kolmogorov (1941a) (k41, red dash line) is given as well as the theoretical prediction of She and Leveque (1994).

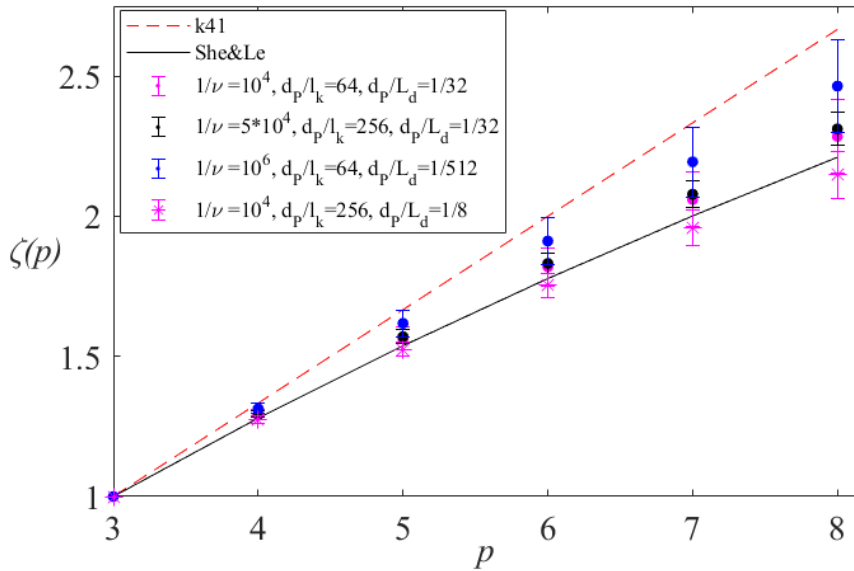


Figure 4.11: Velocity field structure function scaling exponent $\zeta(p)$ for particle laden cases with different Re . For comparison, the non-intermittent prediction of Kolmogorov (1941a) (k41, red dash line) is given as well as the theoretical prediction of She and Leveque (1994).

4.3 Dissipation

4.3.1 Particle size variation: Model A

The model A has been studied for the energy dissipation rate in the presence of particle and compared to the unladen model (Sikiö and Jalali 2014) for Reynolds number $Re \sim 1/\nu = 10^4$. Because of the intermittent characteristic of dissipation signal, in both time and space dimensions, the time average of the spatially resolved energy dissipation rate is considered. A local dissipation maximum is detected in the vicinity of particle surface in all laden cases. The particle size has been discovered to be the effective parameter for the appearance of the dissipation raise near particle surface. The effect of particle on the dissipation spans within 1 to 1.5 particle diameter from the particle surface.

Figures 4.12-4.14 display the time average of the spatially resolved energy dissipation field $\bar{\epsilon}_{N,j}$ for unladen and laden cases in addition to the probability density function (pdf) of the spatially resolved energy dissipation field $\epsilon_{N,j}$ in two spatial locations j , where red is for location near particle and blue for location far from particle for the corresponding cases, shown side by side. The pdf of energy dissipation rate in different spatial locations demonstrates the effect of particle, which is also visible in time averaged spatially resolved dissipation figures. Namely, the dissipation is extended into wider ranges near particle compared to farther locations.

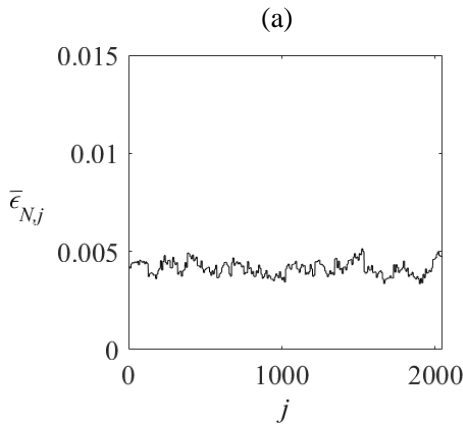


Figure 4.12: The time average of the spatially resolved energy dissipation field of unladen case in model A for $Re \sim 1/\nu = 10^4$.

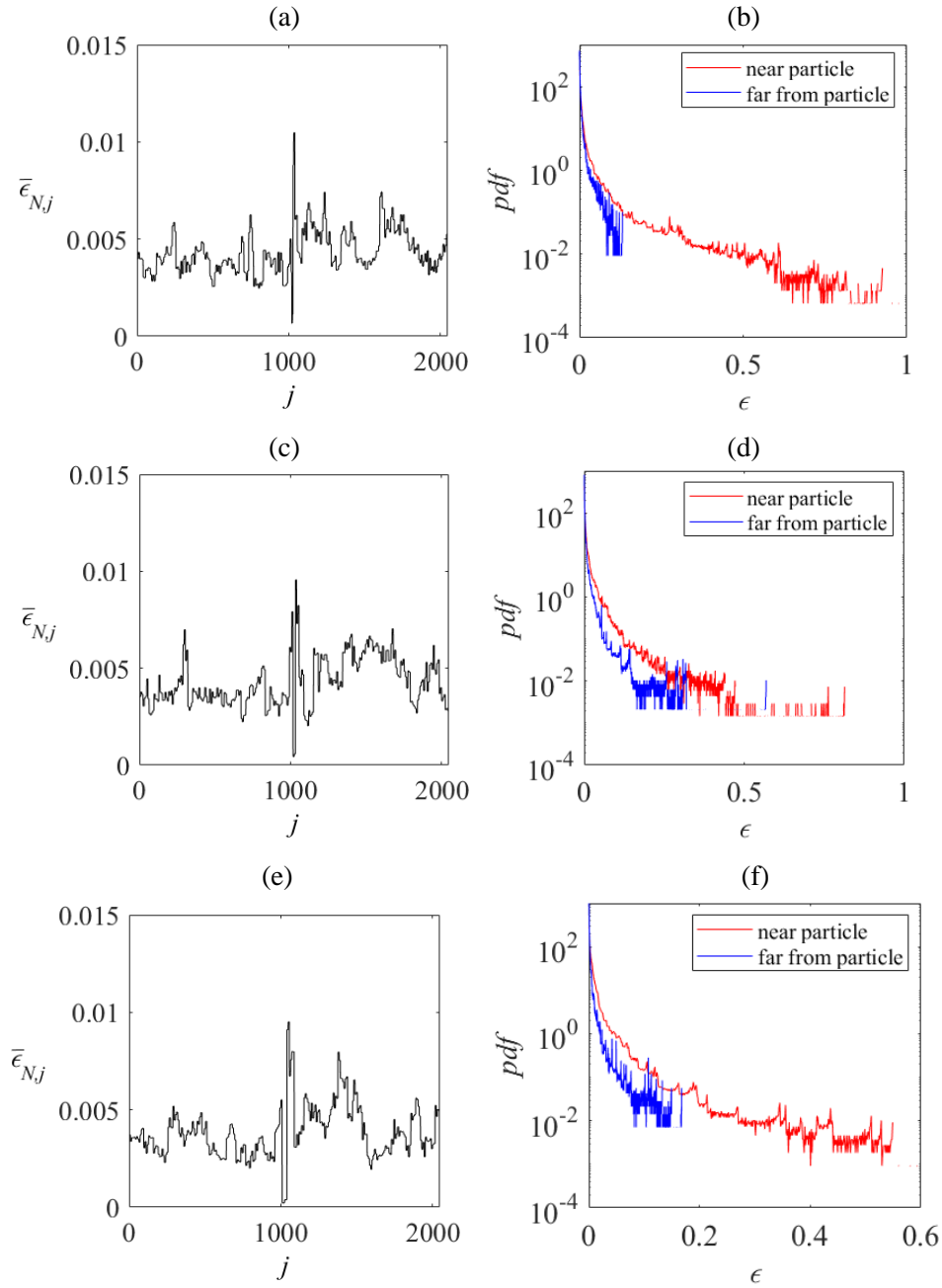


Figure 4.13: The time average of the spatially resolved energy dissipation field $\epsilon_{N,j}$ of laden cases with d_p/l_K as (a) 8, (c) 16, and (e) 32, in model A for $Re \sim 1/\nu = 10^4$. The pdf of the spatially resolved energy dissipation field $\epsilon_{N,j}$ is given in two spatial locations j , where red is for location near particle and blue for location far from particle for the corresponding cases with d_p/l_K as (b) 8, (d) 16, and (e) 32.

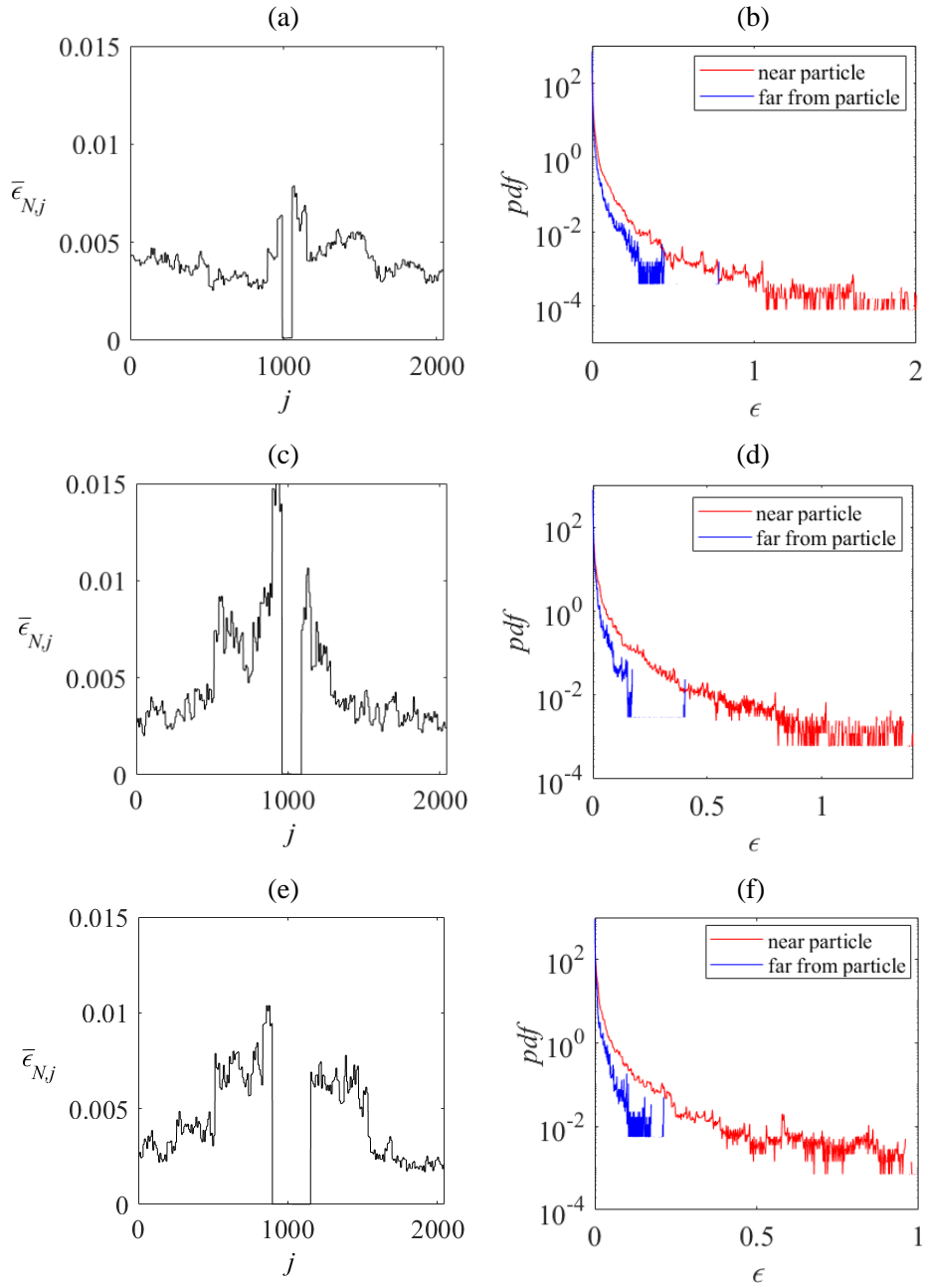


Figure 4.14: The time average of the spatially resolved energy dissipation field $\epsilon_{N,j}$ of laden cases with d_p/l_K as (a) 64, (c) 128, (e) 256 in model A for $Re \sim 1/\nu = 10^4$. The pdf of the spatially resolved energy dissipation field $\epsilon_{N,j}$ is given in two spatial locations j , where red is for location near particle and blue for location far from particle for the corresponding cases with d_p/l_K as (b) 64, (d) 128, (f) 256.

In Fig. 4.15(a), the pdf of the spatially resolved energy dissipation field $\varepsilon_{N,j}$ is presented in which the entire domain of spatial locations is considered (excluding the location of particle) for cases corresponding to Figs. 4.12-4.14. Figure 4.15(b) shows an example of finding the slopes given in Fig. 4.15(a). In model A, the pdf over the entire domain does not display considerable difference between cases. This is due to the lack of horizontal interactions between the model variables in model A, which manifests the effect of particle only in the direct vicinity of particle while farther locations stay untouched. Thus, the pdf over the entire domain does not show any notable difference for different cases.

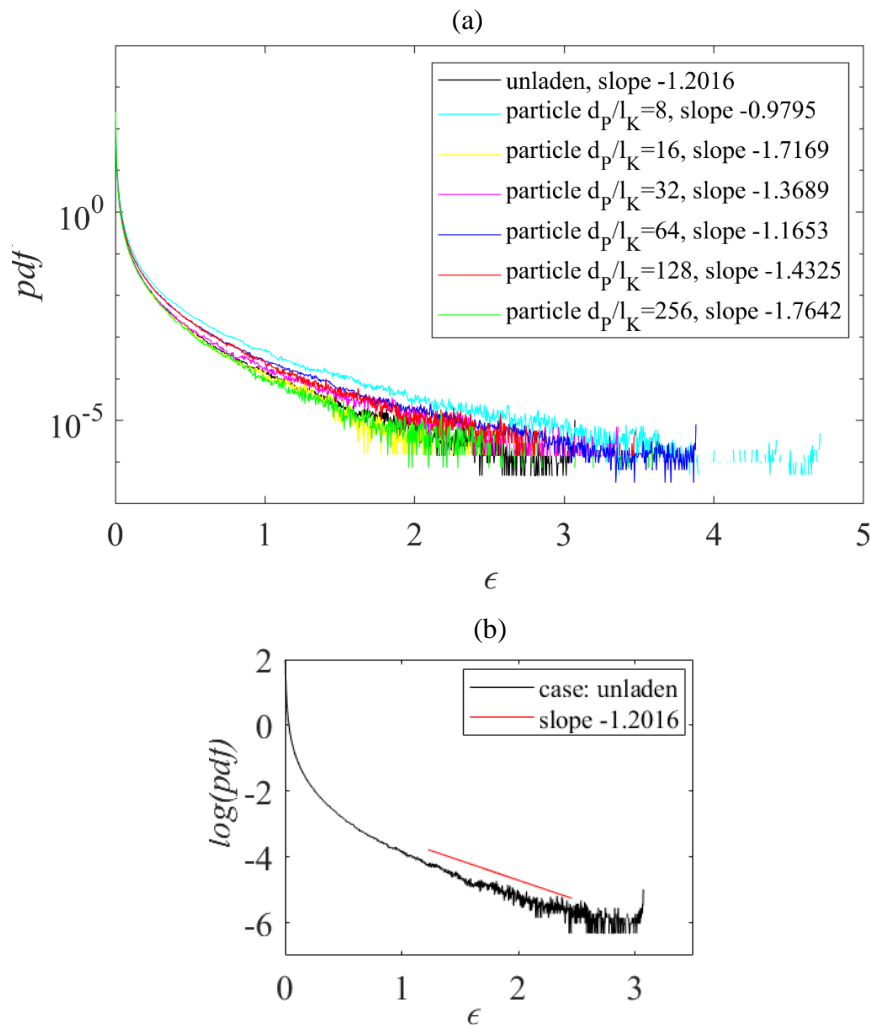


Figure 4.15: (a) The pdf of the spatially resolved energy dissipation field $\varepsilon_{N,j}$, all spatial positions j considered. Unladen and laden cases in model A for $Re \sim 1/\nu = 10^4$. (b) Example of finding the slope, the unladen case.

Table 4.1 presents the standard deviation of the pdf of energy dissipation rate for two spatial locations nearby particle surface, and far from it, as well as for all spatial locations in model A corresponding to $Re^{-1/\nu}=10^4$. The standard deviation is calculated in the tail region of pdf with the cut off value of dissipation as 0.05 for the cases shown in Figs. 4.12-4.15. The standard deviation of dissipation pdf in the location near particle shows bigger values than in the location far from particle, implying to a wider distribution of pdf and higher intermittency near particle. The difference between standard deviation of dissipation pdf in all spatial locations is on the same level for different cases.

Table 4.1: Standard deviation of the pdf of dissipation in particle nearby location and a distant location to particle, as well as all spatial locations in model A for $Re^{-1/\nu}=10^4$, calculated in the tail region of pdf with the cut off value for dissipation as 0.05.

d_P/l_K	near particle	far from particle	all spatial locations considered
unladen			0.031
laden $d_P/l_K=8$	0.079	0.102	0.035
laden $d_P/l_K=16$	0.127	0.037	0.029
laden $d_P/l_K=32$	0.096	0.036	0.027
laden $d_P/l_K=64$	0.040	0.027	0.008
laden $d_P/l_K=128$	0.122	0.066	0.036
laden $d_P/l_K=256$	0.107	0.044	0.026

4.3.2 Particle size variation: Model B

Different size of particles has been investigated in model B to show its effects on energy dissipation locally (Sikiö et al. 2017a, Sikiö et al. 2017b), Reynolds number being $Re^{-1/\nu}=10^4$. Also, the unladen case is included. The time averaged spatially resolved energy dissipation rate field of different cases as well as the pdf of the spatially resolved energy dissipation field ε_{Nj} in two spatial locations j , one near particle surface and the other far from particle, are given in Figs. 4.16-4.17. The mean value corresponding to the unladen case is given for comparison as red dash line in dissipation figures. For model B, the local dissipation maximum is detected in the vicinity of particle in all laden cases. The particle size affects the enlargement of dissipation rate around particle, which is visible in the figures. Higher degree of spatial interaction couplings in model B, in contrast to model A, also increases the efficiency of horizontal energy transfer from the particle surface to farther locations. This leads to the rise of energy dissipation rate in farther locations, compared to the unladen case, which is related to the particle size. Also, the pdf figures reveal the difference between the two chosen spatial locations. Higher dissipation values are detected in the spatial point near particle surface in comparison to the point chosen farther from particle surface.

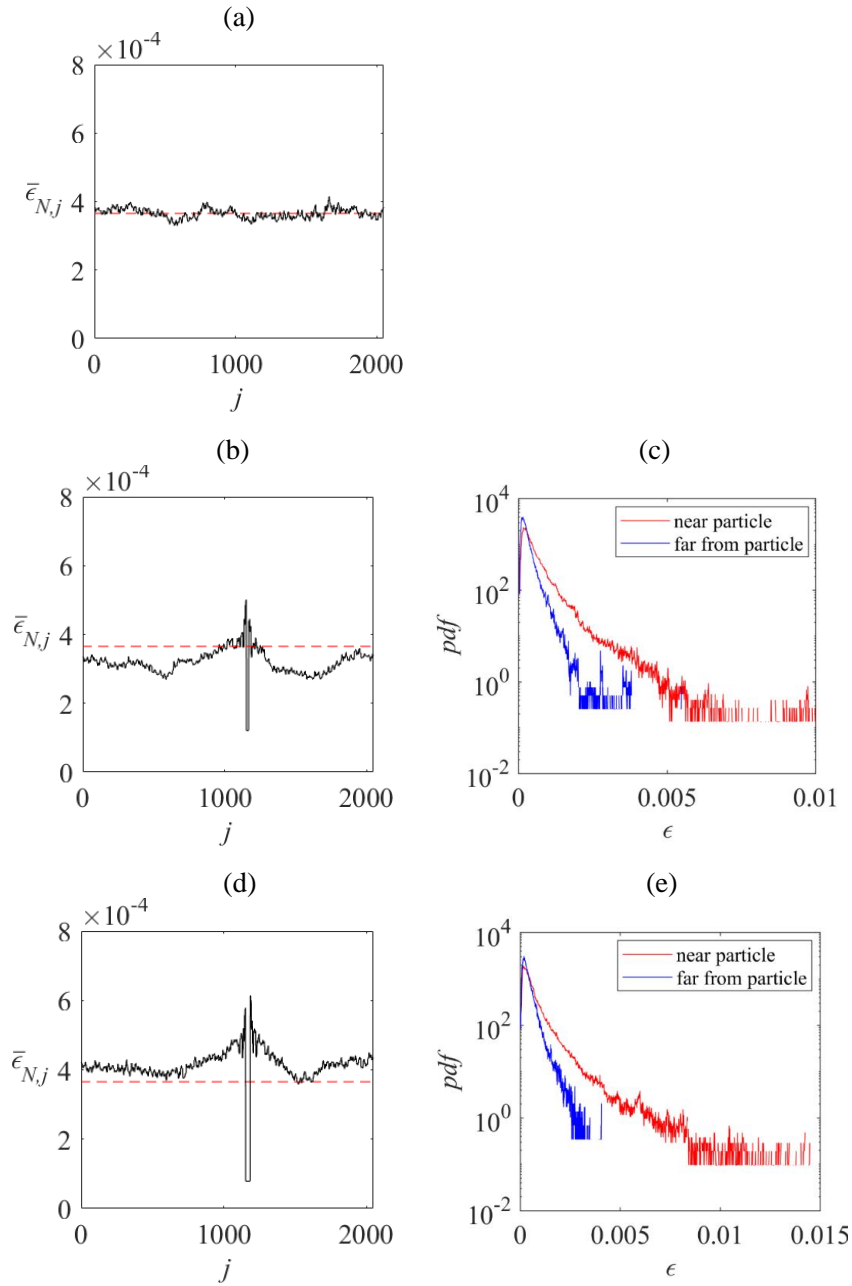


Figure 4.16: The time average of the spatially resolved energy dissipation rate field of a) unladen case, and laden cases with d_p/l_K as b) 16, d) 32, in model B for $Re \sim 1/\nu = 10^4$. The red line indicates the mean value of the unladen case. The pdf of the spatially resolved energy dissipation field is given for the laden cases in two spatial locations j , where red is for location near particle and blue for location far from particle for the corresponding cases with d_p/l_K as c) 16, e) 32.

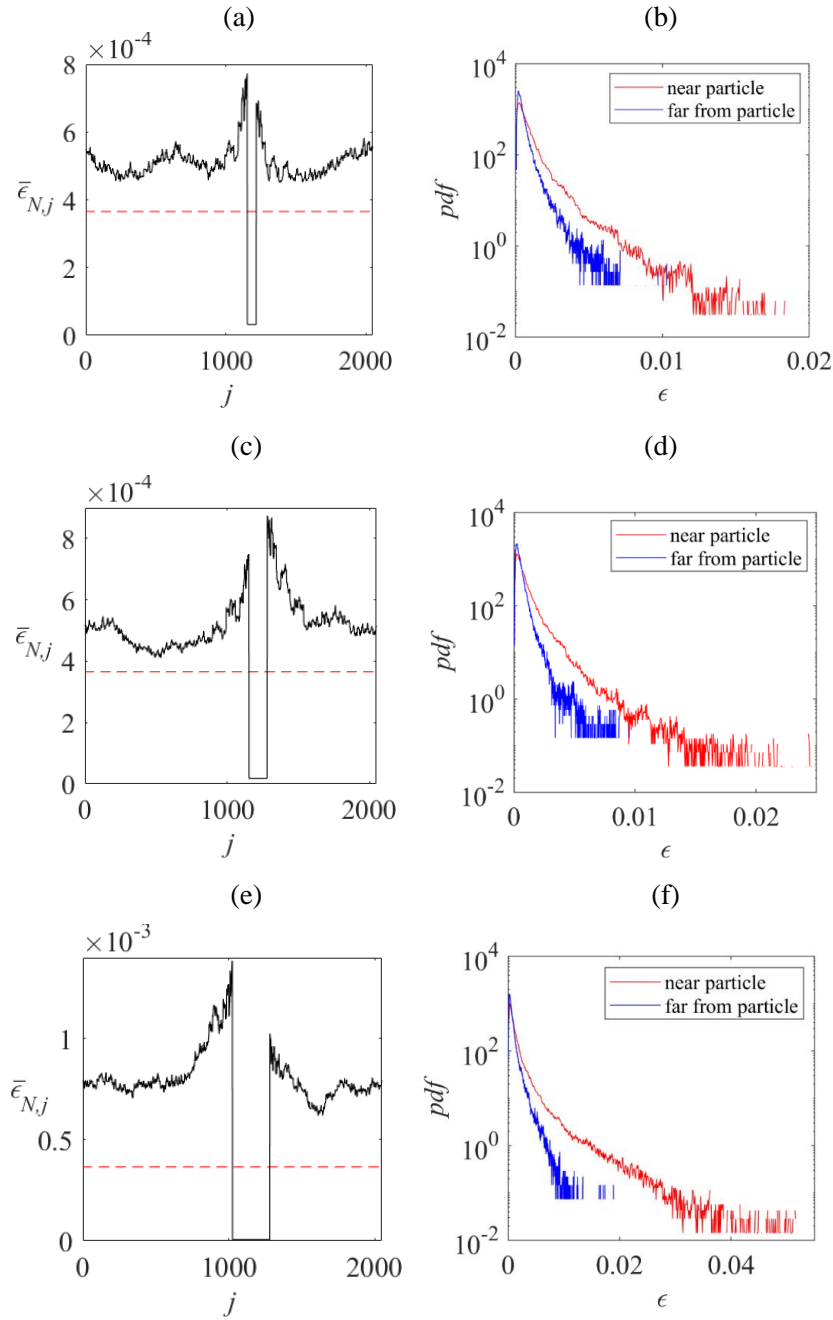


Figure 4.17: The time average of the spatially resolved energy dissipation rate field of laden cases with d_p/l_K as (a) 64, (c) 128, and (e) 256 in model B for $Re \sim 1/\nu = 10^4$. The red line is the mean value corresponding to the unladen case. The pdf of the spatially resolved energy dissipation field is given in two spatial locations j , where red is for location near particle and blue for location far from particle for the corresponding cases with d_p/l_K as (b) 64, d) 128, and f) 256.

In Fig. 4.18(a), the pdf:s of the spatially resolved energy dissipation field $\epsilon_{N,j}$ are demonstrated with considering the whole spatial domain in model B corresponding to the unladen and laden cases in Figs. 4.16-4.17. In Fig. 4.18(b) is given an example of finding the slopes of the pdf curves. The dependence of pdf on the size of particle is detected. In model B, the influence of particle reaches larger range from particle surface due to the horizontal interactions in the model equations, causing more and bigger dissipation bursts in the direct vicinity of particle as well as farther locations.

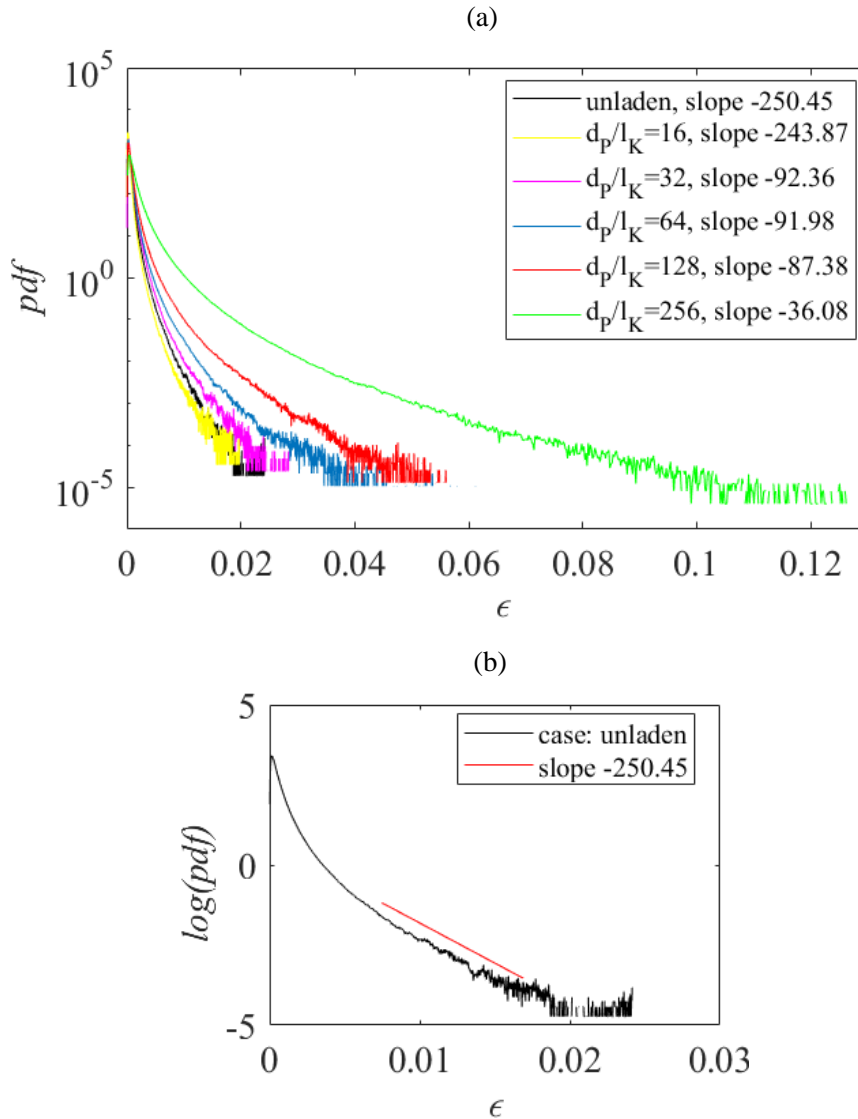


Figure 4.18: (a) The pdf of the spatially resolved energy dissipation field $\epsilon_{N,j}$, all spatial positions considered, for unladen and cases in model B for $Re \sim 1/\nu = 10^4$. (b) Example of finding the slopes.

Table 4.2. Presents the standard deviation of the pdf of energy dissipation for two locations nearby the particle surface, and far from it, as well as for all spatial locations in model B corresponding to $Re \sim 1/\nu = 10^4$. The standard deviation is calculated in the tail region of pdf with the cut off value of dissipation as 0.002 for the cases shown in Figs. 4.16-4.18. The standard deviation of dissipation pdf in the location near particle shows bigger values than in the location far from particle, implying to a wider distribution of pdf and higher intermittency near particle. Also, the bigger the particle, the larger is the standard deviation of dissipation pdf.

Table 4.2: Standard deviation of the pdf of dissipation in particle nearby location and a distant location to particle, as well as all spatial locations in model B for $Re \sim 1/\nu = 10^4$, calculated in the tail region of pdf with the cut off value for dissipation as 0.002.

d_P/l_K	standard deviation of pdf near particle	standard deviation of pdf far from particle	all spatial locations considered
unladen			1.19
laden $d_P/l_K = 16$	4.15	0.45	0.77
laden $d_P/l_K = 32$	7.13	1.92	1.95
laden $d_P/l_K = 64$	6.13	3.15	2.03
laden $d_P/l_K = 128$	8.42	3.58	3.40
laden $d_P/l_K = 256$	8.21	8.07	6.95

4.3.3 Particle pairs

Model B has been studied for particles with variable interparticle distances (Sikiö et al. 2017a). The results are shown in Figs. 4.19-4.20. The distance between particles varied from one to three particle diameters. As for single particle cases, the model shows the augmented energy dissipation rate in the vicinity of particle surfaces for two particles as well. This can be detected in Figs. 4.19(a), (c) and (e), which show the time average of the spatially resolved energy dissipation field $\varepsilon_{N,j}$. In the centre between the particles, the time average of energy dissipation rate displays lower values, which decrease as the distance between particles is increased. The red dash line marks the mean value corresponding to the corresponding unladen case. In Figs. 4.19(b), (d) and (f), the pdf of the spatially resolved energy dissipation field $\varepsilon_{N,j}$ is presented at three spatial locations j for the same cases, from which two are far from particles on the left and right sides and one is between the particles. If the distance between the particles is small (Figs. 4.19(a) and (b)), the pdf of dissipation in location between the particles shows wider range of dissipation values in comparison to the pdf in the farther locations. This difference decreases, if the distance between particles is increased.

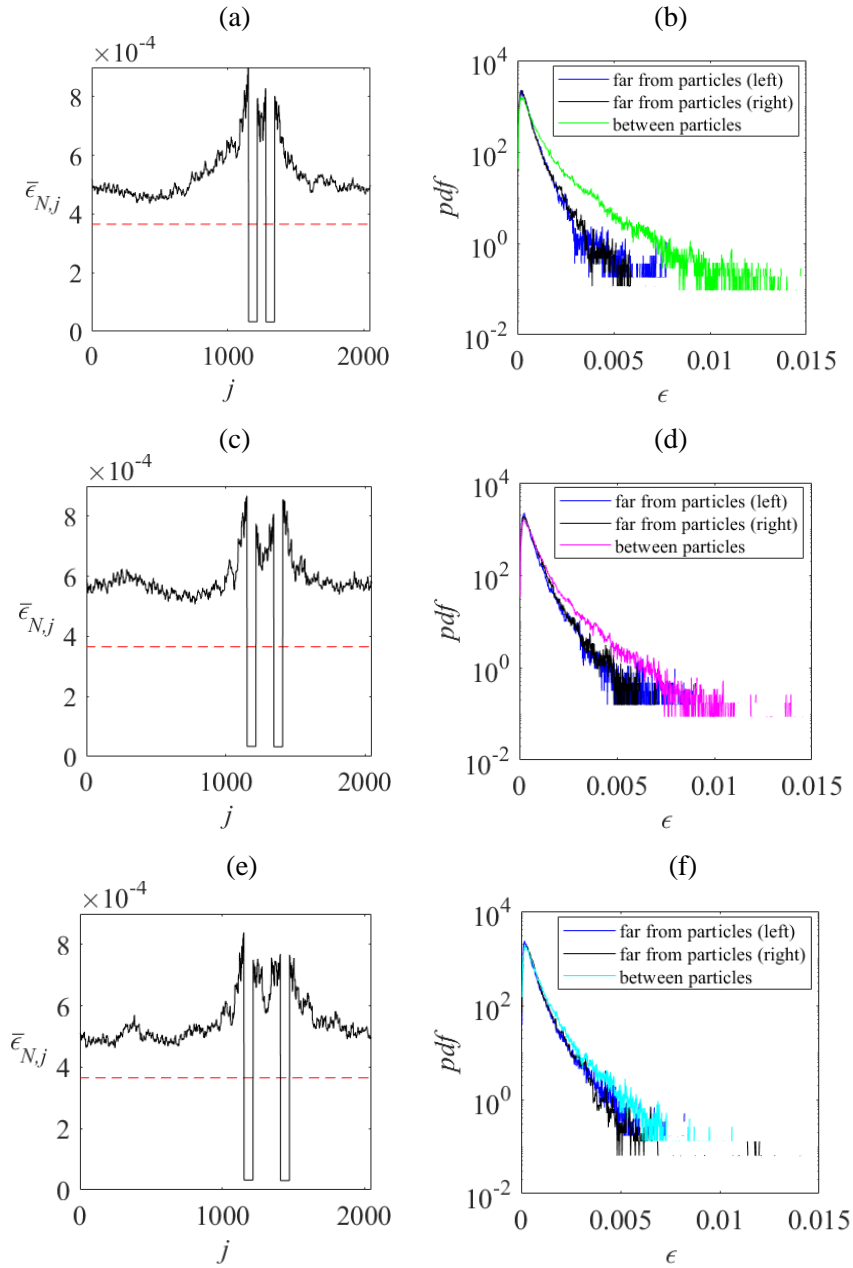


Figure 4.19: The time average of the spatially resolved energy dissipation rate field for cases in model B for $Re \sim 1/\nu = 10^4$, with dual particles with d_p/l_K as 64, with the interparticle distances of (a) $1d_p$, (c) $2d_p$, and (e) $3d_p$, and the pdf of the spatially resolved energy dissipation field $\epsilon_{N,j}$ in three spatial locations j , far from particle on the left and on the right, as well as between the particles for the corresponding cases with d_p/l_K as (b) $1d_p$, (d) $2d_p$, and (f) $3d_p$. The red dash line indicates the mean of the corresponding unladen case.

Figure 4.20(a) shows the pdf:s of the spatially resolved energy dissipation field $\varepsilon_{N,j}$, considering the whole spatial domain, for the cases corresponding to the cases in Fig. 4.19. The pdf of unladen case with same Re is given for comparison. An example of finding the slopes in Fig. 4.20(a) is given in Fig. 4.20(b).

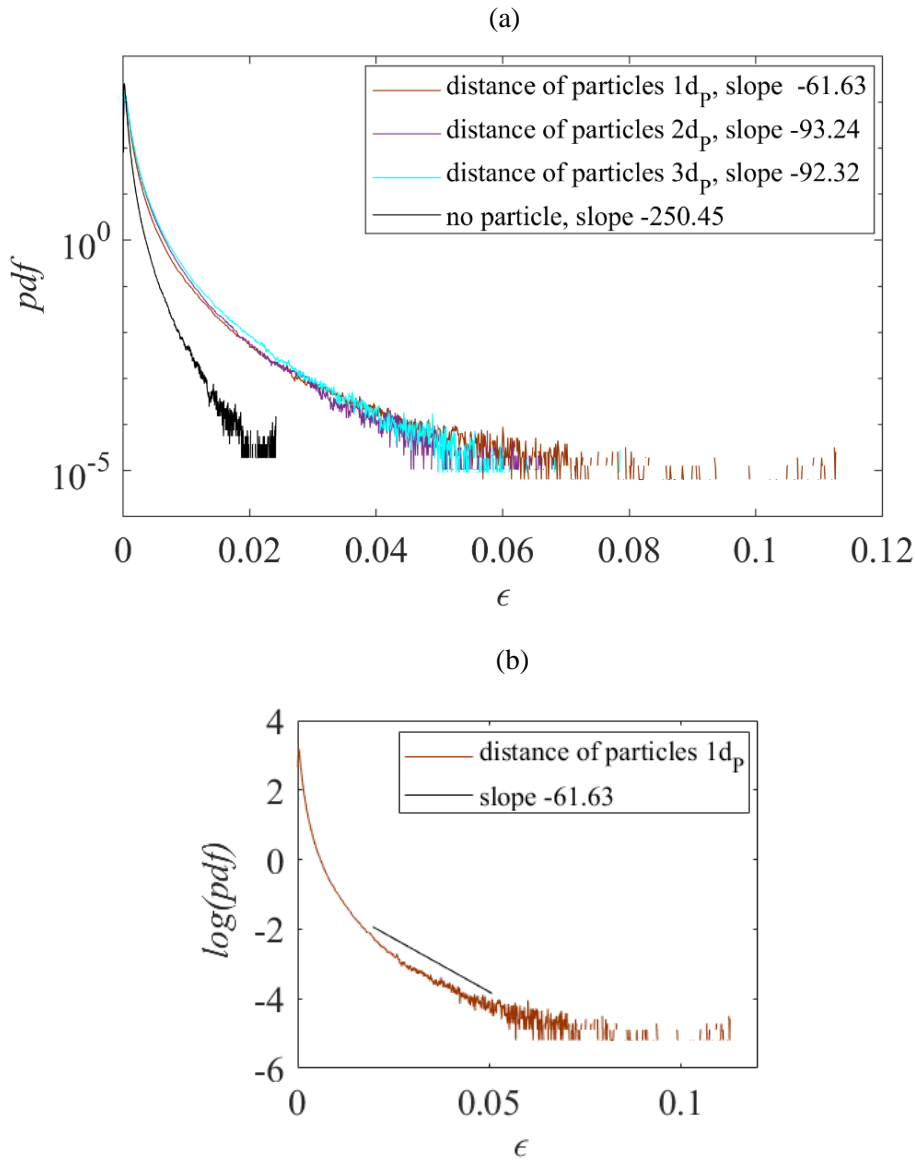


Figure 4.20: (a) The pdf of the spatially resolved energy dissipation field $\varepsilon_{N,j}$, all spatial positions considered, for particle pair cases in model B for $Re \sim 1/\nu = 10^4$. (b) Example of finding the slopes.

Table 4.3 presents the standard deviation of the pdf of energy dissipation for three locations, between the particles and far from it on the left and right, as well as for all spatial locations in model B corresponding to $Re^{-1/\nu}=10^4$. The standard deviation is calculated in the tail region of pdf with the cut off value of dissipation as 0.002 for the cases shown in Fig. 4.9. The standard deviation of dissipation pdf in the location between the particles shows bigger values than in the locations far from particles, implying wider distribution of pdf and higher intermittency between the particles. The smaller the distance between the particles is, the larger standard deviation of dissipation pdf is detected between the particles.

Table 4.3: Standard deviation of the pdf of dissipation in location between the particles and in two distant locations to particles on the left and right, as well as all spatial locations in model B for $Re^{-1/\nu}=10^4$ in the tail region of pdf with the cut off value for dissipation as 0.002.

distance between particles	far from particles, left	far from particles, right	between particles	all spatial locations considered
$1d_p$	3.13	3.37	10.45	2.68
$2d_p$	4.67	5.42	7.69	5.12
$3d_p$	4.84	3.31	6.80	5.17

4.3.4 Variable Reynolds number

Model B is studied with variable Reynolds number, $Re^{-1/\nu}$, as 10^4 , 5×10^4 and 10^6 , in unladen and laden simulations. The time averaged spatially resolved energy dissipation rate of the unladen cases with different Re are shown in Figs. 4.21(a)-(c). The pdf of the spatially resolved energy dissipation field $\varepsilon_{N,j}$ for each unladen case is shown in Fig. 4.21(d), which reveals the dependence of pdf on the Reynolds number. The dissipation is extended into wider ranges in cases with larger Reynolds number.

The particle sizes are chosen such that the cases of various Re can be compared to either particles of same d_p/l_K or particles of same physical size d_p/L_d . Figs. 4.22(a) and (b) show the time averaged spatially resolved energy dissipation rate of the cases with the same d_p/l_K , namely 256 and $Re^{-1/\nu}$ as 10^4 and 5×10^4 , respectively. In Figs. 4.22(c) and (d), are shown the cases with $d_p/l_K=64$ and $Re^{-1/\nu}$ is 10^4 and 10^6 , respectively. It can be seen in these figures that if the particle size in proportion to l_K is kept constant, larger dissipation boost near particle surface is detected for smaller Re . On the other hand, if the particle size in proportion to the domain size is kept constant, which is the circumstance in cases shown in Figs. 4.22(b) and (c), the dissipation boost near particle is similar for cases with differing Re .

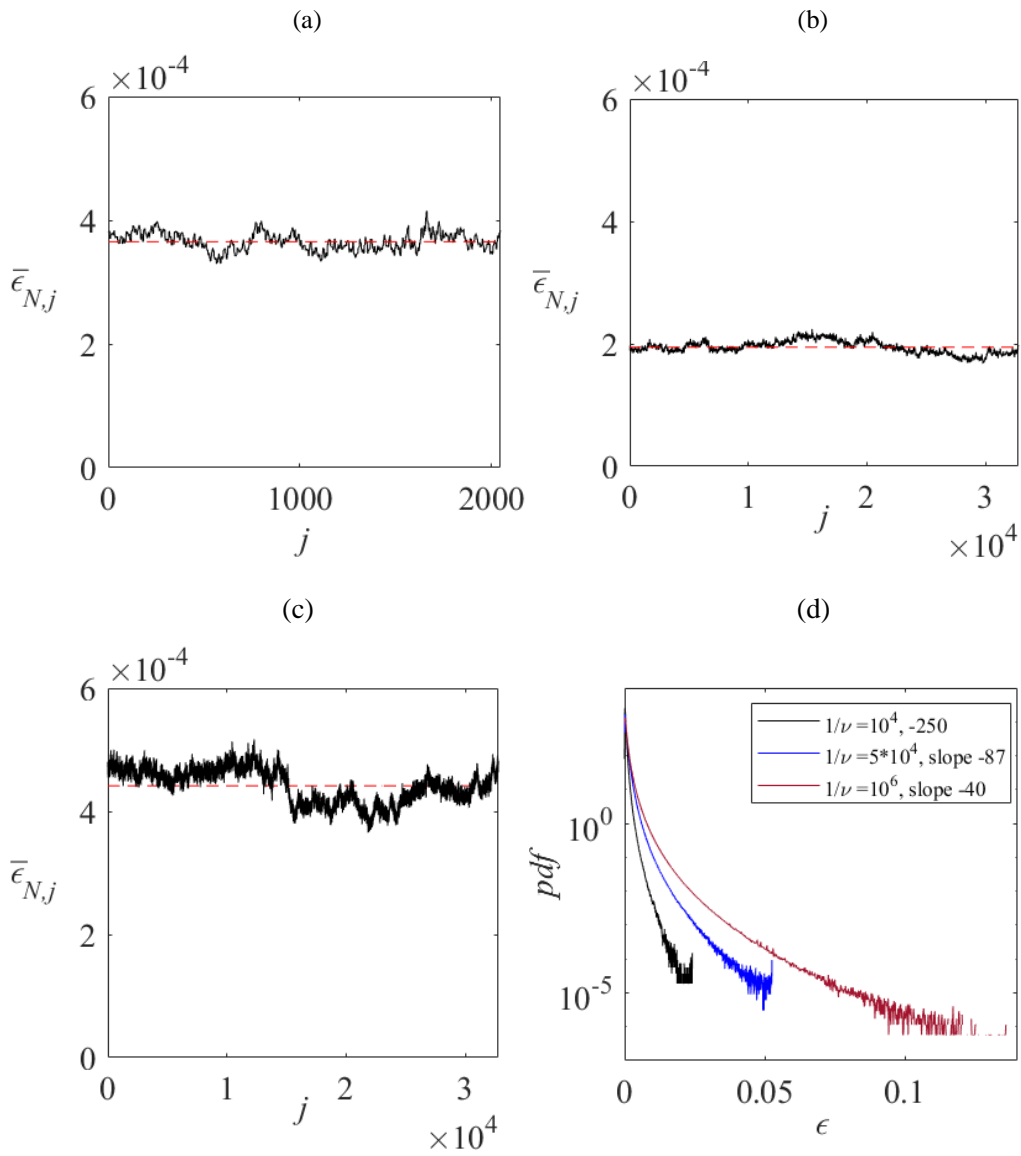


Figure 4.21: The time average of the spatially resolved energy dissipation field $\epsilon_{N,j}$ for unladen cases with $Re \sim 1/\nu$ as (a) 10^4 , (b) 5×10^4 , (c) 10^6 , where the red line indicates the mean, and (d) the pdf of the spatially resolved energy dissipation field $\epsilon_{N,j}$, all spatial positions considered, for the cases considered in (a)-(c).

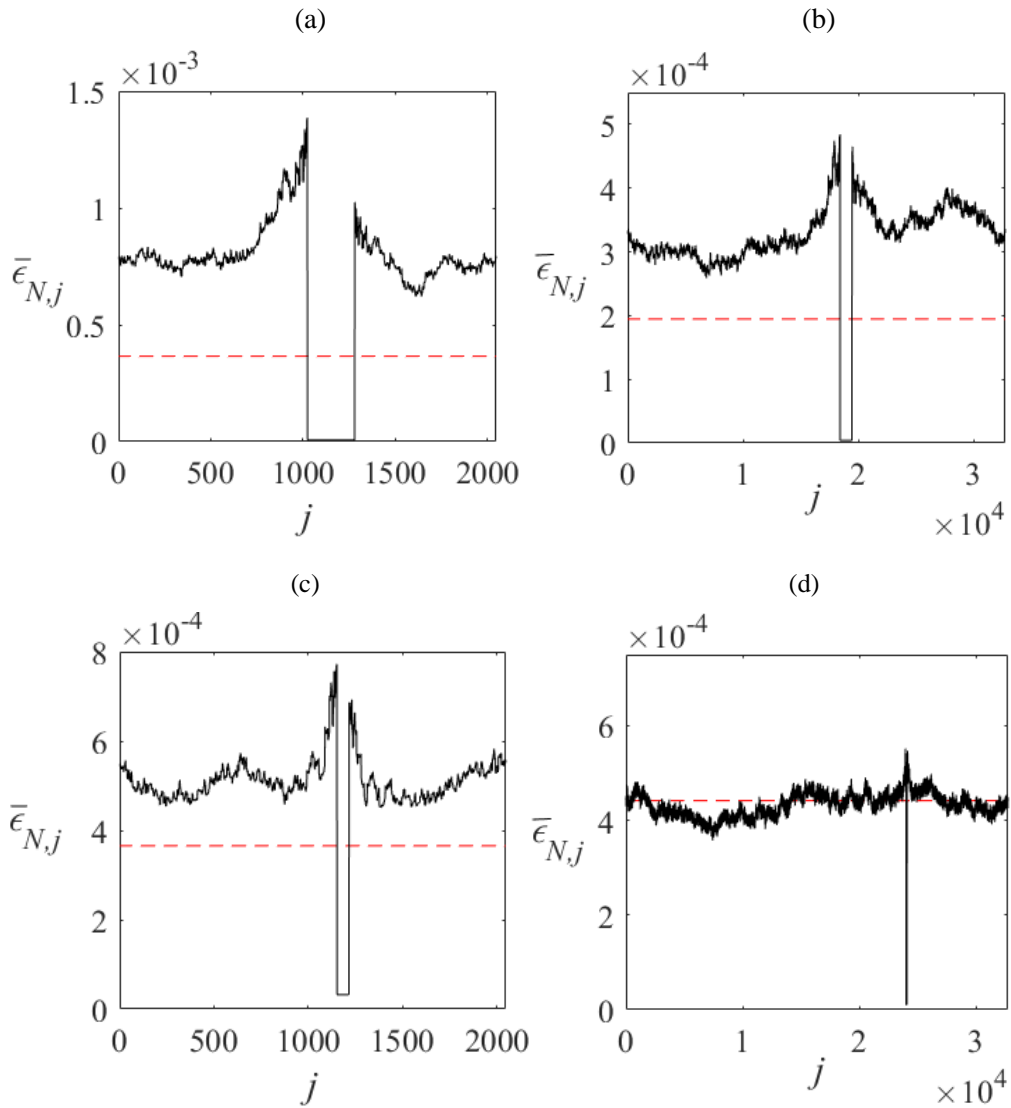


Figure 4.22: The time average of the spatially resolved energy dissipation field $\epsilon_{N,j}$ for laden cases with (a) $Re \sim 1/\nu = 10^4$, $d_p/l_K = 256$, and $d_p/l_K = 1/8$, (b) $Re \sim 1/\nu = 5 \times 10^4$, $d_p/l_K = 256$ and $d_p/l_K = 1/32$, (c) $Re \sim 1/\nu = 10^4$, $d_p/l_K = 64$ and $d_p/l_K = 1/32$, (d) $Re \sim 1/\nu = 10^6$, $d_p/l_K = 64$ and $d_p/l_K = 1/512$.

Figure 4.23. shows the pdf of the spatially resolved energy dissipation field $\epsilon_{N,j}$ in two spatial locations j , one near particle surface and the other far from particle for the laden cases introduced in Fig. 4.22. In these figures, it can be observed that the particle size in proportion to the domain size is the dominant factor in determining the separation between the pdf of dissipation at locations near particle and far from particle. For bigger particles, the dissipation is extended into wider ranges near particle compared to the farther locations.

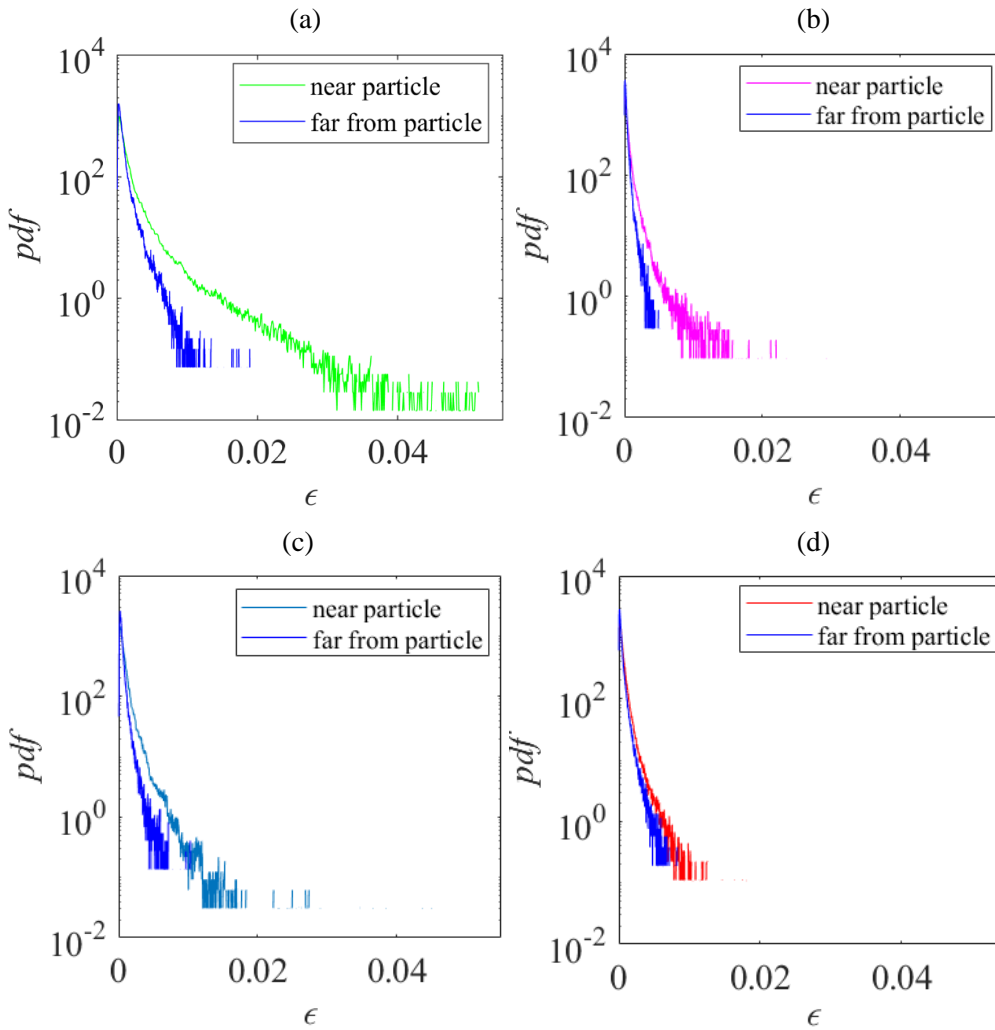


Figure 4.23: The pdf of the spatially resolved energy dissipation field $\epsilon_{N,j}$ in two spatial locations j near the particle surface and far from particle for the cases introduced in Fig. 4.22 with (a) $Re^{-1}/\nu=10^4$, $d_P/l_K=256$ and $d_P/L_d=1/8$, (b) $Re^{-1}/\nu=5\times 10^4$, $d_P/l_K=256$ and $d_P/L_d=1/32$, (c) $Re^{-1}/\nu=10^4$, $d_P/l_K=64$ and $d_P/L_d=1/32$, (d) $Re^{-1}/\nu=10^6$, $d_P/l_K=64$ and $d_P/L_d=1/512$.

Figure 4.24 shows the pdf:s of the spatially resolved energy dissipation field $\varepsilon_{N,j}$, considering all the spatial locations j , in unladen and laden cases with variable Reynolds numbers corresponding to the cases shown in Figs. 4.21 and 4.22. The dependence of pdf on Reynolds number is visible. Also, it can be seen, that the dissipation is extended into wider ranges in laden cases compared to the corresponding unladen case with same Re . This is valid for different Re .

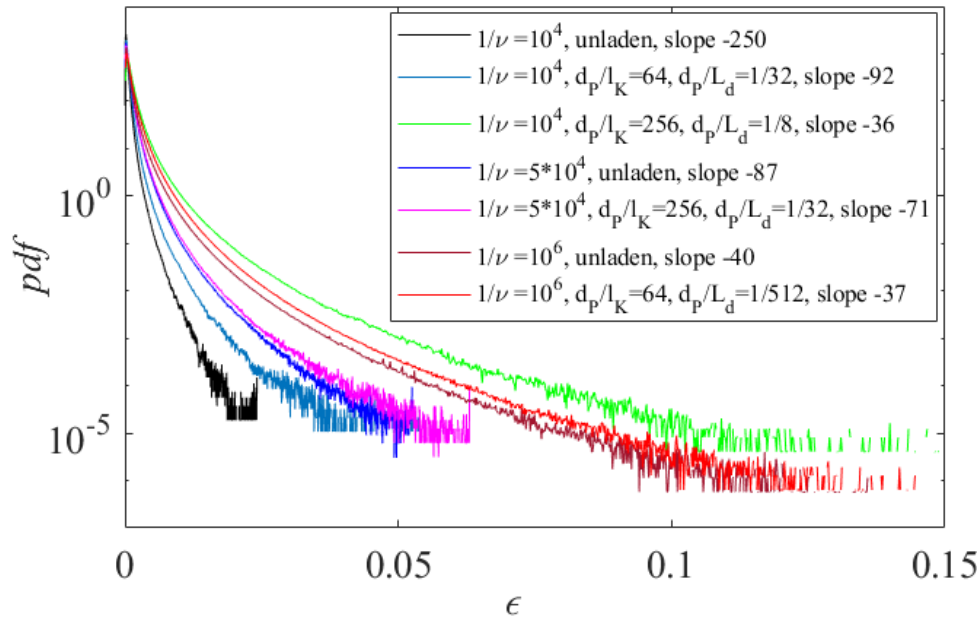


Figure 4.24: (a) The pdf of the spatially resolved energy dissipation field $\varepsilon_{N,j}$, all spatial positions j considered, for unladen cases and laden cases with different Re .

Table 4.4 presents the standard deviation of the pdf of energy dissipation for two locations nearby particle surface, and far from it, as well as for all spatial locations in model A corresponding to three Reynolds numbers $Re \sim 1/\nu$, 10^4 , 5×10^4 and 10^6 . The standard deviation is calculated in the tail region of pdf with the cut off value of dissipation as 0.002 for the cases shown in Figs. 4.23-4.24. Unladen cases for higher $Re \sim 1/\nu$ as 5×10^4 and 10^6 , have larger standard deviation of the dissipation pdf than the case with lower Re . In laden cases, the standard deviation of dissipation pdf in the location near particle shows bigger values than in the location far from particle, implying to a wider distribution of pdf and higher intermittency near particle.

Table 4.4: Standard deviation of the pdf of dissipation in particle nearby location and a distant location to particle as well as all spatial locations in model B for three Re , calculated in the tail region of pdf with the cut off value for dissipation as 0.002.

	near particle	far from particle	all spatial locations
unladen $Re \sim 1/\nu = 10^4$			1.19
unladen $Re \sim 1/\nu = 5 \times 10^4$			4.17
unladen $Re \sim 1/\nu = 10^6$			3.36
laden $Re \sim 1/\nu = 10^4$, $d_P/l_K = 256$, $d_P/L_d = 1/8$	8.21	8.07	6.95
laden $Re \sim 1/\nu = 5 \times 10^4$, $d_P/l_K = 256$, $d_P/L_d = 1/32$	3.97	1.38	4.05
laden $Re \sim 1/\nu = 10^4$, $d_P/l_K = 64$, $d_P/L_d = 1/32$	6.13	3.15	2.03
laden $Re \sim 1/\nu = 10^6$, $d_P/l_K = 64$, $d_P/L_d = 1/512$	4.34	2.81	5.25

5 Conclusions

In this thesis, the (1+1)-dimensional hierarchical shell model (tree model) (Benzi et al. 1997) has been modified for the insertion of dispersed phase particles in 1D turbulent field. The tree model can express temporal as well as spatial intermittency of turbulence. It can reach high Reynolds numbers with less computational cost than other methods, such as DNS. Here, the performance of modified tree model system has been investigated in long period of time using two models, namely A and B, which differ in the range of spatial interactions. The only modification due to the insertion of a solid obstruction, called particle, in the model domain is associated with setting the variables to zero in the spatial location of particle for all the scales of particle diameter and less. Variable finite particle sizes larger than Kolmogorov length scale have been considered with particle diameters between 8 and 256 times of the Kolmogorov length scale corresponding to the range of $1/512$ to $1/8$ of the integral length scale. Furthermore, variable Reynolds numbers, $Re \sim 1/\nu$ as 10^4 , 5×10^4 and 10^6 , have been considered.

The direct comparison of shell model results with the experimental results of real 3D turbulent flow with moving particles is not reasonable. However, the shell models share many features with real turbulence. In real physics, turbulence modulation resulting from the interaction between finite size of particle and turbulence can be observed as dissipation upsurge in the vicinity of particle surface. In this study, a solid obstacle fixed in space, has been introduced in hierarchical shell model. It has been shown, that this model produces this aspect of particle turbulence interaction as increased dissipation near the particle surface.

The results of model A have been compared to the DNS results of Burton and Eaton with matching simulation configuration of a fixed particle under decaying turbulence condition. For shell model this setting has a rather low Reynolds number, which leads to relatively short inertial range of energy cascade. Also, the particle size is rather small compared to the Kolmogorov length scale ($d_p = 2l_K$). This means that synchronization, i.e. similar behaviour of nearby variables, which affects the last dissipative levels, is effective on the scale of particle size in this case. However, the tree model results display the increase of the energy dissipation rate close to the particle surface. This result is in accordance with the DNS results of Burton and Eaton, with only minor differences in the level of dissipation escalation near the surface, which is smaller in tree model simulations. The performance of model B was compared to model A in similar set of simulations with larger particle and larger Reynolds number. For model B, the dissipation escalation is smaller than in model A. This can be related to different interaction range in spatial direction. In model A, interactions among variables are mainly vertical, while model B also includes horizontal couplings improving the energy transfer in spatial direction from particle surface to further locations. This can be noticed in slightly elevated dissipation levels in farther locations from the particle surface compared to the corresponding unladen cases. Also, computational fluid dynamics (CFD) simulations have been performed using the computer package of ANSYS-Fluent. Several simulations were conducted in accordance with the conditions of DNS simulations in Burton and Eaton

(2005) using k -epsilon, k -omega and 7-equation Reynolds Stress turbulence models. In comparison to the results of Burton and Eaton, the Fluent simulations were found slightly overestimating the dissipation rise near the surface.

The scaling properties of the models for unladen and particle laden cases have been considered via calculating velocity field structure functions. The existence of a solid obstruction causes local perturbations among the scales. Thus, the structure functions are defined for a location j in space as well as for the entire spatial domain. The local structure functions have been defined either in nearby location or in far location to the particle surface, and studied for models A and B. In model A, increased intermittency has been detected in nearby location to particle surface and decreased intermittency in farther locations, when compared to the unladen case or laden case all spatial positions considered. However, in model B, only minor differences have been detected in local scaling effects between nearby and farther locations. Models A and B differ in number of horizontal interactions among the shell variables. In model A, the disturbance resulted in a particle insertion can be seen only in direct vicinity of the particle surface due to the lack of horizontal interactions. In model B, the horizontal interactions are activated and the local disturbance has been found to affect the farther locations as well.

The velocity field structure functions in all spatial locations have been studied in unladen and laden simulations of models A and B. Both unladen and laden simulation results of models A and B have been found to be in good agreement with the numerical results of Benzi et al. (1997). The results have been compared to the non-intermittent prediction of Kolmogorov (1941a) and intermittent prediction of She and Leveque (1994), which revealed the intermittent characteristics of both unladen and laden simulations in models A and B. The degrees of intermittency are different in models A and B, which can be assigned to different interaction range in physical space. Model A is found to be more intermittent than model B, as was observed also by Benzi et al. (1997) for unladen cases, and this has been found to be valid for the particle laden results as well. Furthermore, model B has been studied for scaling in the presence of variable size of particles. It has been realized that the scaling is in line with the results of unladen simulations. For larger particles, a deviation towards more intermittent regime has been observed. The anomalous scaling exponent has been extracted for the simulation results of model B with three different Reynolds numbers in unladen and particle laden cases. Intermittency of each case has been found to be in the same level with only minor differences. The only major difference has been found in physical size variation of the particle which creates more intermittent regime as particle size grows.

Turbulent energy dissipation rate is looked through the time-average of the spatially resolved energy dissipation rate. The turbulent modulation due to the particle insertion in the turbulent domain is detected as augmented dissipation in spatial locations near particle surface in the range of 1-1.5 particle diameters of the particle surface. Particle size affects the amount of the dissipation rise for both models A and B. Also, particle pairs located in a relative distance of one to three particle diameters are studied in model B. Augmented energy dissipation rate was discovered near the surfaces of both particles. In the midpoint

of particles, the energy dissipation rate decreases as the interparticle distance increases. Furthermore, for variable Reynolds numbers, larger dissipation boost near particle surface is observed for smaller Re , if the particle size in proportion to l_K is kept constant. However, for cases with same particle physical size, dissipation boost near particle surface is similar for different Reynolds numbers.

Furthermore, the effect of particle on the turbulent energy dissipation field has been studied through the probability density function (pdf) of the spatially resolved energy dissipation field $\varepsilon_{N,j}$ in separate spatial locations, nearby the particle and far from particle surface, as well as in all spatial locations. Pdf of intermittent signal tends to develop stretched tails with large deviations from the average value caused by very strong events. Pdf study revealed, that dissipation was extended into more wider ranges near particle than in the further locations. Pdf of the spatially resolved dissipation considering all spatial positions showed difference between model A and model B. In model A, the strong dissipation bursts occur near the particle surface. Whereas, in model B, large-amplitude events are detected mostly at the particle surface, but also in further locations. In model B, the pdf of the dissipation in all spatial locations generates longer tails in particle laden cases than in the unladen case and the extreme tail becomes stronger as the particle size is increased. Furthermore, stronger tails in pdf of dissipation are detected as the Reynolds number is increased.

The results revealed, that the tree model is capable of reproducing the enhancement of energy dissipation in the close locations of the solid region introduced in the model. It should be noted that the only modification to the original tree model is that the velocity variables of the cells within the location of particle are zeroed. Comparison with the DNS results of Burton and Eaton (2005) indicated that the tree model underestimates the dissipation boost near the particle. This could be made up by a supplementary source term for dissipation at the particle surface. However, further studies are required to adjust such source term in the scale of particle size, which is acting in same manner as forcing term. Also, the comparison between tree model results and results of Burton and Eaton (2005) raised some difficulties due to the relatively low Reynolds number and small particle size of the simulation case of Burton and Eaton (2005). The tree model is developed for the study of high Re turbulence in one spatial dimension and time. The existing results of local energy dissipation effects near particle surface are restricted to rather low Reynolds numbers. Further studies of experimental and computational methods are advisable for more precise validation of the model in high Re cases.

References

- S. Balachandar and J. K. Eaton (2010). *Turbulent dispersed multiphase flow*. Annual Review of Fluid Mechanics, 42, pp. 111-133.
- R. Benzi, L. Biferale, R. M. Kerr and E. Torvatore (1996). *Helical shell models for three-dimensional turbulence*. Physical Review E, 53, pp. 3541-3550.
- R. Benzi, L. Biferale, R. Tripicciono and E. Trovatore (1997). *(1+1)-dimensional turbulence*. Physics of Fluids, 9 (8), pp. 2355-2363.
- R. Benzi, S. Ciliberto, R. Tripicciono, C. Baudet, F. Massaioli and S. Succi (1993). *Extended self-similarity in turbulent flows*. Physical Review E, 48 (1), pp. R29-32.
- L. Biferale (2003). *Shell Models of Energy Cascade in Turbulence*. Annual Review of Fluid Mechanics, 35(1), pp. 441-468.
- L. Biferale, G. Boffetta, and B. Gastaing (2003). Fully developed turbulence. In: R. Livi and A. Vulpiani, eds, *The Kolmogorov legacy in physics. Lecture notes in physics*, 636, pp. 149-172. New York: Springer-Verlag Berlin Heidelberg.
- L. Biferale and R. M. Kerr (1995). *Role of inviscid invariants in shell models of turbulence*. Physical Review E, 52, pp. 6113-6122.
- T. Bohr, M. H. Jensen, G. Paladin and A. Vulpiani (1998). *Dynamical systems approach to turbulence*. New York: Cambridge University Press. ISBN 9780521475143. 372 p.
- M. Bourgoin and H. Xu (2014). *Focus on dynamics of particles in turbulence*. New Journal of Physics, 6, pp 085010:1-9.
- J. Boussinesq (1877). *Theorie de l'Écoulement Tourbillant*. Mémoires présentés par divers savants à l'Académie des Sciences, 23, pp. 1-680.
- J. C. Brändle de Motta, J.-L. Estivalezes, E. Climent, and S. Vincent (2016). *Local dissipation properties and collision dynamics in a sustained homogeneous turbulent suspension composed of finite size particles*. International Journal of Multiphase Flow, 85, pp. 369-379.
- T. M. Burton and J. K. Eaton (2005). *Fully resolved simulations of particle-turbulence interaction*. Journal of Fluid Mechanics, 545, pp. 67-111.
- P. Chou (1945). *On velocity correlations and the solutions of the equations of turbulent fluctuation*. Quarterly of Applied Mathematics, 3(1), pp. 38-54.

- M. Cisse, H. Homann, and J. Bec (2013). *Slipping motion of large neutrally buoyant particles in turbulence*. Journal of Fluid Mechanics, 735, pp. 1-10.
- V. N. Desnyansky and E. A. Novikov (1974). *Simulation of cascade processes in turbulent flows*. Journal of Applied Mathematics and Mechanics (Prikl. Mat. Mekh.), 38 (3), pp. 507-513.
- P. D. Ditlevsen (2011). *Turbulence and shell models*. Cambridge: Cambridge University Press, ISBN 9780521190367. 152 p.
- G. L. Eyink (2007-2008) *Turbulence Theory*, course notes, The Johns Hopkins University, Intermittency & Anomalous Scaling: chapter IIIc: (D) Empirical Results on Turbulence Scaling of Velocity Increments.
- R. T. Fisher et al (2008). *Terascale turbulence computation using the FLASH3 application framework on the IBM Blue Gene/L system*, IBM Journal of Research and Development, 52(½), pp. 127-136.
- U. Frisch (1995). *Turbulence the legacy of A.N. Kolmogorov*, Cambridge University Press, Cambridge. ISBN 0-521-45713- 0, 296 p.
- E. B. Gledzer (1973). *System of hydrodynamic type admitting two quadratic integrals of motion*. Soviet Physics Doklady, 18, pp. 216-217.
- M. M. Hoque, S. Mitra, M. J. Sathe, J. B. Joshi, G. M. Evans (2016). *Experimental investigation on modulation of homogeneous and isotropic turbulence in the presence of single particle using time-resolved PIV*. Chemical Engineering Science, 22, Vol.153, pp.308-329.
- W. Hwang and J. K. Eaton (2006) *Turbulence attenuation by small particles in the absence of gravity*. Intl J. Multiphase Flow, 32, pp. 1386–1396.
- M. H. Jensen, G. Paladin and A. Vulpiani (1991). *Intermittency in a cascade model for three dimensional turbulence*. Physical Review A, 43(2), pp. 798-805.
- J. Jimenez (2004). *The contributions of A. N. Kolmogorov to the theory of turbulence*. Arbor CLXXVIII, 704, pp. 589-606.
- L. P. Kadanoff, D. Lohse, J. Wang and R. Benzi (1995). *Scaling and dissipation in the GOY shell model*. Physics of Fluids, 7(3), pp. 617-629.
- A.N. Kolmogorov (1941a). *The local structure of turbulence in incompressible viscous fluids at very large Reynolds numbers*, Dokl. Akad. Nauk. SSSR, 30, pp. 299-303. Reprinted in Proc. R. Soc. London A, 434, pp. 9-13.

- A.N. Kolmogorov (1941b). *On the degeneration of isotropic turbulence in an incompressible viscous fluids*, Dokl. Akad. Nauk. SSSR, 31, pp. 538-541.
- A.N. Kolmogorov (1941c). *Dissipation of energy in isotropic turbulence*. Dokl. Akad. Nauk. SSSR, 32, pp. 19-21.
- A. N. Kolmogorov (1942). *Equations of Turbulent Motion of an Incompressible Fluid*. Izvestia Academy of Sciences, USSR; Physics, 6, (1, 2), pp. 56-58.
- J.G. M. Kuerten (2016), *Point-Particle DNS and LES of Particle-Laden Turbulent flow - a state-of-the-art review*. Flow, Turbulence and Combustion, 97(3), pp. 689-713.
- B. E. Launder, and D. B. Spalding (1972). *Mathematical Models of Turbulence*. Academic Press, London/New York, England, 169p.
- E.N. Lorenz (1972). *Low-order models representing realizations of turbulence*. J. Fluid Mech., 55(3), pp. 545-563.
- F. Lucci, A. Ferrante, S. Elghobashi (2010). *Modulation of isotropic turbulence by particles of Taylor length-scale size*. Journal of Fluid Mechanics, 650, pp. 5-55.
- J. L. Lumley and A. M. Yaglom (2001). *A Century of Turbulence*. Flow Turbulence and Combustion, 66(3), pp. 241-286.
- E. E. Michaelides, C. T. Crowe and J. D. Schwarzkopf, eds. (2017). *Multiphase Flow Handbook*, Second edition. Taylor & Francis Group, CRC Press, United Kingdom. ISBN-13 978-1-4987-0101-3. 1394 p.
- J. F. Muzy, E. Bacry and A. Arneodo (1993). *Multifractal formalism for fractal signals: the structure functions approach versus the wavelet-transform modulus-maximum method*. Physical Review E, 47, pp. 875-844.
- T. Nakano (1988). *Direct interaction approximation of turbulence in the wave packet representation*. Physics of Fluids, 31, pp. 1420-1428.
- A. Naso and A. Prosperetti (2010). *The interaction between a solid particle and a turbulent flow*. New Journal of Physics, 12, pp. 033040: 1-20.
- K. Ohkitani and M. Yamada (1989). *Temporal intermittency in the energy cascade process and local Lyapunov analysis in fully developed model turbulence*. Progress of Theoretical Physics, 81(2), pp. 329-341.
- J. O'Neil and C. Meneveau (1993). *Spatial correlations in turbulence: Predictions from the multifractal formalism and comparison with experiments*. Physics of Fluids A, 5, pp. 158-172.

- C. Poelma, and G. Ooms (2006). *Particle-turbulence interaction in a homogeneous, isotropic turbulent suspension*. Applied Mechanics Reviews, 59(2), pp. 78-90.
- A. Pouquet, C. Gloaguen, J. Leorat, R. Grappin (1984). *A Scalar Model of MHD Turbulence*. Chaos and Statistical Methods, 24, pp. 206-210.
- L. Prandtl (1925). *Über die ausgebildete Turbulenz*. Zeitschrift für angewandte Mathematik und Mechanik, 5(2), pp. 136-139.
- O. Reynolds (1883). *An experimental investigation of the circumstances which determine whether the motion of water shall be direct or sinuous, and of the law of resistance in parallel channels*. Philosophical Transaction Royal Society of London, 174, pp. 935-982.
- O. Reynolds (1895). *On the Dynamical Theory of Incompressible Viscous Fluids and the Determination of the Criterion*. Philosophical Transactions of the Royal Society of London. A, 186, pp. 123-164.
- L. F. Richardson (1922). *Weather Prediction by Numerical Process*. Cambridge (University Press). 236 p.
- J. P. Richter and R. C. Bell (1970). *The Notebooks of Leonardo da Vinci, Volume 2*, Courier Corporation, (transl. Ugo Piomelli in J.L. Lumley (1992). *Some comments on turbulence*. Physics of Fluids A, 4, pp. 203-211).
- J. Rotta (1951). *Statistische theorie nichthomogener turbulenz*. Zeitschrift für Physik A, 129(6), pp. 547-572.
- A. Saber, T.S. Lundström, and J.G.I. Hellström (2015). *Turbulent Modulation in Particulate Flow. A Review of Critical Variables*. Engineering, 7, pp. 597-609.
- Z. She and E. Leveque (1994). *Universal scaling laws in fully developed turbulence*. Physic. Rev. Lett. 72(3), pp. 336-339.
- E.D. Siggia (1978). *Model of intermittency in three-dimensional turbulence*. Physical review A, 17(3), pp. 1166-1176.
- P. Sikiö and P. Jalali (2014). *Study of turbulent energy dissipation rate of fluid flow in the vicinity of dispersed phase boundary using spatiotemporal tree model*. Chaos 24(4), pp. 043139 (1-11).
- P. Sikiö, T. Tynjälä and P. Jalali (2017a). *A spatiotemporal tree model for turbulence in dispersed phase multiphase flows: Energy dissipation rate (EDR) behavior in single particle and binary particles arrays*. Chaos 27, pp. 013102 (1-10).

- P. Sikiö, T. Tynjälä, and P. Jalali (2017b). *Effect of particle size on scaling properties of turbulence: Shell model approach*. Submitted for journal publication.
- P. Sikiö, T. Tynjälä, and P. Jalali (2017c). *Turbulent energy dissipation rate modification due to particle insertion: Effect of Reynolds number*. Submitted for journal publication.
- J. Smagorinsky (1963). *General Circulation Experiments with the Primitive Equations*. Monthly Weather Review 91(3), pp. 99–164.
- P. R. Spalart, W-H. Jou, M. Strelets, and S. R. Allmaras (1997). Comments on the feasibility of LES for wings, and on a hybrid RANS/LES approach. In: C. Liu, and Z. Liu, eds, *Advances in DNS/LES, 1st AFOSR International Conference on DNS/LES*, pp. 137-47. Columbus, OH: Greyden Press.
- S. Sundaram and L. R. Collins (1999). *A numerical study of the modulation of isotropic turbulence by suspended particles*. Journal of Fluid Mechanics, 379, pp. 105-143.
- T. Tanaka and J. K. Eaton (2010). *Sub-Kolmogorov resolution particle image velocimetry measurements of particle-laden forced turbulence*. Journal of Fluid Mechanics, 643, pp. 177-206.
- H. Tennekes, J. L. Lumley (1972). *A First course in turbulence*. The MIT press, Cambridge, Massachusetts and London, England, 300p.
- R. Volk, E. Calzavarini, G. Verhille, D. Lohse, N. Mordant, J.-F. Pinton, and F. Toschi (2008). *Acceleration of heavy and light particles in turbulence: Comparison between experiments and direct numerical simulations*. Physica D, 237, pp. 2084-2089.
- L.-P. Wang, O. Ayala, H. Gao, C. Andersen, and K. L. Mathews (2014). *Study of forced turbulence and its modulation by finite-size solid particles using the lattice Boltzmann approach*. Computers and Mathematics with Applications, 67(2), pp. 363-380.

ACTA UNIVERSITATIS LAPPEENRANTAENSIS

741. YLI-HUUMO, JESSE. The role of technical dept in software development. 2017. Diss.
742. LAYUS, PAVEL. Usability of the submerged arc welding (SAW) process for thick high strength steel plates for Arctic shipbuilding applications. 2017. Diss.
743. KHAN, RAKHSHANDA. The contribution of socially driven businesses and innovations to social sustainability. 2017. Diss.
744. BIBOV, ALEKSANDER. Low-memory filtering for large-scale data assimilation. 2017. Diss.
745. ROTICH, NICOLUS KIBET. Development and application of coupled discrete and continuum models in solid particles classification. 2017. Diss.
746. GAST, JOHANNA. The coopetition-innovation nexus: Investigating the role of coopetition for innovation in SMEs. 2017. Diss.
747. KAPOOR, RAHUL. Competition and disputes in the patent life cycle. 2017. Diss.
748. ALI-MARTTILA, MAAREN. Towards successful maintenance service networks – capturing different value creation strategies. 2017. Diss.
749. KASHANI, HAMED TASALLOTI. On dissimilar welding: a new approach for enhanced decision-making. 2017. Diss.
750. MVOLA BELINGA, ERIC MARTIAL. Effects of adaptive GMAW processes: performance and dissimilar weld quality. 2017. Diss.
751. KARTTUNEN, JUSSI. Current harmonic compensation in dual three-phase permanent magnet synchronous machines. 2017. Diss.
752. SHI, SHANSHUANG. Development of the EAST articulated maintenance arm and an algorithm study of deflection prediction and error compensation. 2017. Diss.
753. CHEN, JIE. Institutions, social entrepreneurship, and internationalization. 2017. Diss.
754. HUOTARI, PONTUS. Strategic interaction in platform-based markets: An agent-based simulation approach. 2017. Diss.
755. QU, BIN. Water chemistry and greenhouse gases emissions in the rivers of the "Third Pole" / Water Tower of Asia". 2017. Diss.
756. KARHU, PÄIVI. Cognitive ambidexterity: Examination of the cognitive dimension in decision-making dualities. 2017. Diss.
757. AGAFONOVA, OXANA. A numerical study of forest influences on the atmospheric boundary layer and wind turbines. 2017. Diss.
758. AZAM, RAHAMATHUNNISA MUHAMMAD. The study of chromium nitride coating by asymmetric bipolar pulsed DC reactive magnetron sputtering. 2017. Diss.
759. AHI, MOHAMADALI. Foreign market entry mode decision-making: Insights from real options reasoning. 2017. Diss.
760. AL HAMDI, ABDULLAH. Synthesis and comparison of the photocatalytic activities of antimony, iodide and rare earth metals on SnO₂ for the photodegradation of phenol and its intermediates under UV, solar and visible light irradiations. 2017. Diss.

761. KAUTTO, JESSE. Evaluation of two pulping-based biorefinery concepts. 2017. Diss.
762. AFZALIFAR, ALI. Modelling nucleating flows of steam. 2017. Diss.
763. VANNINEN, HEINI. Micromultinationals - antecedents, processes and outcomes of the multinationalization of small- and medium-sized firms. 2017. Diss.
764. DEVIATKIN, IVAN. The role of waste pretreatment on the environmental sustainability of waste management. 2017. Diss.
765. TOGHYANI, AMIR. Effect of temperature on the shaping process of an extruded wood - plastic composite (WPC) profile in a novel post-production process. 2017. Diss.
766. LAAKKONEN, JUSSI. An approach for distinct information privacy risk assessment. 2017. Diss.
767. KASURINEN, HELI. Identifying the opportunities to develop holistically sustainable bioenergy business. 2017. Diss.
768. KESKISAARI, ANNA. The impact of recycled raw materials on the properties of wood - plastic composites. 2017. Diss.
769. JUKKA, MINNA. Perceptions of international buyer-supplier relational exchange. 2017. Diss.
770. BAYGILDINA, ELVIRA. Thermal load analysis and monitoring of doubly-fed wind power converters in low wind speed conditions. 2017. Diss.
771. STADE, SAM. Examination of the compaction of ultrafiltration membranes with ultrasonic time-domain reflectometry. 2017. Diss.
772. KOZLOVA, MARIIA. Analyzing the effects of a renewable energy support mechanism on investments under uncertainty: case of Russia. 2017. Diss.
773. KURAMA, ONESFOLE. Similarity based classification methods with different aggregation operators. 2017. Diss.
774. LYYTIKÄINEN, KATJA. Removal of xylan from birch kraft pulps and the effect of its removal on fiber properties, colloidal interactions and retention in papermaking. 2017. Diss.
775. GAFUROV, SALIMZHAN. Theoretical and experimental analysis of dynamic loading of a two-stage aircraft engine fuel pump and methods for its decreasing. 2017. Diss.
776. KULESHOV, DMITRII. Modelling the operation of short-term electricity market in Russia. 2017. Diss.
777. SAARI, JUSSI. Improving the effectiveness and profitability of thermal conversion of biomass. 2017. Diss.
778. ZHAO, FEIPING. Cross-linked chitosan and β -cyclodextrin as functional adsorbents in water treatment. 2017. Diss.
779. KORHONEN, ILKKA. Mobile sensor for measurements inside combustion chamber – preliminary study. 2017. Diss.

